Water Resources Research

RESEARCH ARTICLE
10.1029/2023WR035149

2D and 3D Computational Modeling of Surface Flooding in Urbanized Floodplains: Modeling Performance for Various Building Layouts

Xuefang Li[1], Guilhem Dellinger[2], Sébastien Erpicum[3], Lihua Chen[1], Shuyue Yu[1], Léo Guiot[2], Pierre Archambeau[3], Michel Pirotton[3], and Benjamin Dewals[3]

[1]Guangxi Key Laboratory of Disaster Prevention and Engineering Safety, Guangxi University, Nanning, China, [2]ICube Laboratory, National School for Water and Environmental Engineering, Strasbourg, France, [3]Hydraulics in Environmental and Civil Engineering (HECE), University of Liège (ULiège), Liège, Belgium

Key Points:

- Predictions of 2D and 3D computational models were compared against laboratory experiments representing urban flooding in a steady-state
- Both models perform equally well to predict upstream flow depth, outlet discharge partition, and velocity field in street networks
- In urban layouts with large open spaces, only the 3D model accurately predicts the velocity field

Supporting Information:

Supporting Information may be found in the online version of this article.

Correspondence to:

L. Chen and X. Li,
xdslclh@gxu.edu.cn;
lxuefangcn@gxu.edu.cn

Citation:

Li, X., Dellinger, G., Erpicum, S., Chen, L., Yu, S., Guiot, L., et al. (2024). 2D and 3D computational modeling of surface flooding in urbanized floodplains: Modeling performance for various building layouts. *Water Resources Research*, *60*, e2023WR035149. https://doi.org/10.1029/2023WR035149

Received 24 APR 2023
Accepted 27 MAR 2024

Author Contributions:

Conceptualization: Guilhem Dellinger, Benjamin Dewals
Data curation: Guilhem Dellinger, Shuyue Yu, Léo Guiot
Formal analysis: Lihua Chen, Benjamin Dewals
Funding acquisition: Lihua Chen, Michel Pirotton, Benjamin Dewals
Investigation: Guilhem Dellinger, Léo Guiot
Methodology: Guilhem Dellinger, Sébastien Erpicum, Benjamin Dewals

Abstract Understanding the strengths and limitations of the modeling capacity of surface flooding in urbanized floodplains is of utmost importance as such events are becoming increasingly frequent and extreme. In this study, we assess two computational models against laboratory observations of surface urban flooding in a reduced-scale physical model of idealized urban districts. Four urban layouts were considered, involving each three inlets and three outlets as well as a combination of three- and four-branch crossroads together with open spaces. The first model (2D) solves the shallow-water equations while the second one (3D) solves the Reynolds-averaged Navier-Stokes equations. Both models accurately predict the flow depths in the inlet branches. For the discharge partition between the outlets, deviations between the computations and laboratory observations remain close to the experimental uncertainties (maximum 2.5 percent-points). The velocity fields computed in 3D generally match the measured surface velocity fields. In urban layouts involving mostly a network of streets, the depth-averaged velocity fields computed by the 2D model agree remarkably well with those of the 3D model, with differences not exceeding 10%, despite the presence of helicoidal flow (revealed by the 3D computations). In configurations with large open areas, the 3D model captures generally well the trajectory and velocity distribution of main surface flow jet and recirculations; but the 2D model does not perform as well as it does in relatively channelized flow regions. Visual inspection of the jet trajectories computed by the 2D model in large open areas reveals that they substantially deviate from the observations.

Plain Language Summary Advancing our modeling capacity of urban flooding is of utmost importance for improving the design of risk reduction measures. During extreme urban flooding, complex flow patterns develop in urban environments, involving three-dimensional flow structures. Though, urban floods are commonly simulated with two-dimensional computational models. So far, no detailed comparison between flow fields predicted by two- and three-dimensional computational models were conducted and assessed against reference data such as experimental observations for representative configurations of urban flooding. In this study, we assess two computational models against laboratory observations of urban flooding in a reduced-scale physical model of an idealized district.

1. Introduction

Worldwide, rapid urbanization and more frequent extreme rainfall events increase the frequency and severity of urban floods (Chen et al., 2015; Fang, 2016; Hettiarachchi et al., 2018), such as the disastrous events of July 2021 in Zhengzhou, China (Guo et al., 2023) and in Europe, particularly in Germany and Belgium (Bosseler et al., 2021; Fekete & Sandholz, 2021). Urban floods cause huge economic losses and a high number of fatalities (Kreibich et al., 2019; Lv et al., 2022). Flood risk modeling and management is thus a high priority for sustainable urban management (Guo et al., 2021; Rosenzweig et al., 2021). The focus is set here on surface urban flooding, as typically encountered in the case of riverine floods affecting urbanized floodplains. Urban flood flows are particularly complex due to the multiple pathways typically present in urban environments, such as in street networks (Luo et al., 2022). Therefore, advancing the understanding of flow processes in an urban district is of utmost importance for improving the accuracy of management tools, such as computational models predicting hazard and risk (Mignot and Dewals, 2022).

Project administration: Lihua Chen, Michel Pirotton, Benjamin Dewals
Resources: Lihua Chen, Pierre Archambeau, Michel Pirotton, Benjamin Dewals
Software: Guilhem Dellinger, Sébastien Erpicum, Léo Guiot, Pierre Archambeau
Supervision: Sébastien Erpicum, Lihua Chen, Benjamin Dewals
Validation: Shuyue Yu
Visualization: Shuyue Yu
Writing – review & editing: Guilhem Dellinger, Sébastien Erpicum, Lihua Chen, Shuyue Yu, Pierre Archambeau, Benjamin Dewals

Urban flow paths are generally shaped by the arrangement of obstacles, such as building blocks, in the floodplains (Leandro et al., 2016). Since the flow aspect ratio (depth to width ratio) reaches relatively high values during extreme events (Mignot et al., 2006; Paquier et al., 2020), shallow water flow conditions may not be prevailing and three-dimensional flow structures are likely to develop (Mignot et al., 2013; Rong et al., 2020). However, so far, no detailed comparisons between flow fields predicted by two- (2D) and three-dimensional (3D) computational models were conducted and assessed against reference data such as experimental observations for representative configurations of urban flooding.

Several studies explored the 3D flow structure in single open-channel junctions or bifurcations using detailed laboratory experiments or 3D computational modeling.

- Weber et al. (2001) used an acoustic Doppler velocimeter (ADV) to perform velocity and turbulence measurements in a laboratory model of a single 90° junction. The compiled dataset was later used for assessing computational models. Using a commercial computational fluid dynamics (CFD) code, Chen et al. (2017) obtained good predictions of the observed flow characteristics, with mean absolute percentage error of respectively 5%, 10% and 18% for water surface elevation, longitudinal velocity and transverse velocity. Based on a different commercial CFD model, Luo et al. (2018) also found a good agreement between the experimental and the numerical results concerning the main features in the primary flow, secondary flow, turbulent kinetic energy, and water surface variations. Both Chen et al. (2017) and Luo et al. (2018) adopted the volume of fluid technique to track the water surface variations.
- Based on another experimental facility of a single 90° junction, Mignot et al. (2012) conducted ADV measurements revealing the evolution of streamwise velocity distributions along the main channel. They tested the same 3D CFD model as used by Chen et al. (2017), but they adopted the rigid lid approximation for defining the water surface. Computed magnitude, size, and spatial positioning of most flow structures were well reproduced by the computations, except for the extent of the main recirculation zone which was overestimated in the near-bed region.
- Mignot et al. (2013) applied particle image velocimetry (PIV) to measure horizontal velocity fields in a 90° bifurcation model and they investigated the influence of square obstacles on flow patterns, but 3D flow structures were not explored and only 2D computations were performed.
- Schindfessel et al. (2015) applied surface particle tracking velocimetry (PTV) and ADV to shed light on the flow structures developing in a 90° junction with a chamfered cross-section and a high lateral inflow (up to 95% of total inflow). Compared to the case of a lower lateral inflow, the experimental observations, combined with large eddy simulations (LES), revealed a recirculating eddy in the upstream branch, stronger helicoidal cells and zones of upwelling flow downstream of the flow intersection.
- Momplot et al. (2017) carried out experiments in a three-branch bifurcation model. By combining 3D simulations and experimental visualization of streamlines using dye injection, they discovered a helix-shaped vertical recirculation downstream of the side branch for certain combinations of Froude number and aspect ratio of the upstream channel.

In these studies, considerable efforts were made to explore flow surface velocity pattern or three-dimensional flow structures, but they are all restricted to a single junction or bifurcation. In contrast, the case of a more comprehensive street network has not received the same attention.

Studies covering (parts of) an urban district focused mostly on analyzing water levels, discharge partition between the streets, and in some cases the distribution of surface velocity (Dewals et al., 2023; Finaud-Guyot et al., 2018, 2019; Li, Erpicum, et al., 2021; Li et al., 2022b; Mejia-Morales et al., 2021; Mejía-Morales et al., 2023; Testa et al., 2007; Velickovic et al., 2017; Zhu et al., 2023).

- Based on a 5 m by 5 m experimental setup representing a network of 14 streets, with 49 crossroads, Finaud-Guyot et al. (2018) focused mostly on analyzing the discharge partition between the street branches, but the entire surface velocity field was not mapped in 2D.
- Based on a 3D computational model, Zhu et al. (2023) investigated flood discharge intrusion into groups of buildings of various layouts. However, the analyses were focused mostly on flow exchange and danger for pedestrians, while details of the flow structures were not characterized.
- In a street network involving two inlet branches and three outlet branches, Mejia-Morales et al. (2021) experimentally analyzed the influence of flow intrusion into building blocks on flow processes. By mapping the surface velocity obtained by large-scale particle image velocimetry (LSPIV), they revealed large

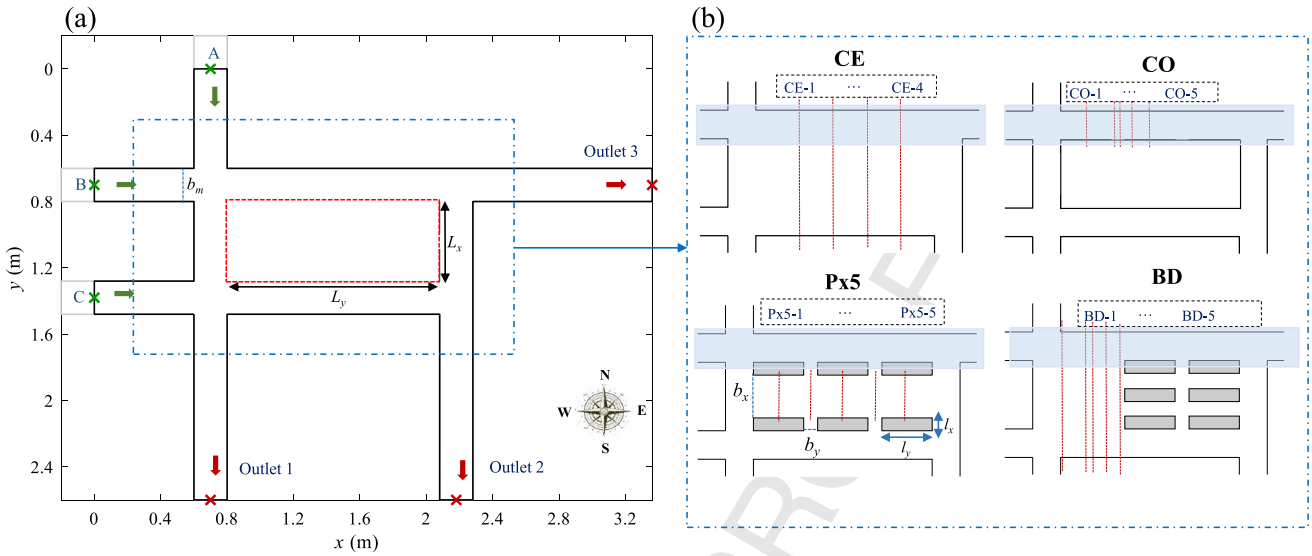

Figure 1. (a) Geometry of urban forms. The red dashed rectangle shows the central open space where the building blocks are positioned, $L_x = 0.48$ m, $L_y = 1.28$ m. Bold black lines sketch the domain used for numerical modeling; (b) sketch of the four tested urban configurations. In panel (b), the blue-shaded areas correspond street B3 (referred to in Section 3.3).

horizontal recirculations, which hint at the plausible presence of three-dimensional flow structures such as secondary currents. The same configurations were simulated by two computational models, but only in 2D and 3D flow features were not analyzed (Dewals et al., 2023).

- Li, Erpicum, et al. (2021) conducted experiments in five geometric configurations representing idealized urban layouts. In most parts of street networks, strong similarities were found between depth-averaged flow velocity computed in 2D and measured surface velocity; but significant deviations between computations and observations of the flow field were obtained downstream of contraction zones and in configurations involving relatively large open areas (e.g., representing a square in a real urban area). These differences hint at possible limitations of the 2D computational model, and they highlight the need for 3D modeling to disclose the reasons for deviations between computed and measured velocities.

The present study aims at investigating urban flow patterns and structures in a part of a street network using both 2D and 3D modeling, as well as experimental observations. To complement the 2D modeling and the experimental data of Li, Erpicum, et al. (2021), new 3D flow computations were performed in four geometric configurations representing various urban settings, using the open-source computational fluid dynamics model OpenFOAM. Systematic comparisons between the outcomes of 2D and 3D simulations as well as the laboratory observations are performed for the first time for urban flood conditions in a series of geometric layouts. The comparisons cover inlet flow depths, partitions of outflow discharge at the outlets, as well as measured surface velocity, depth-averaged velocity computed in 2D, as well as depth-averaged and surface velocity fields computed in 3D. Three-dimensional flow structures are revealed based on the results of the 3D simulations.

From an engineering perspective, this study contributes to informing practitioners on the need to opt for 3D modeling depending on the type of urban topography and the flow variables of interest. It also points at which flow variables computed by 2D models can be safely trusted in engineering practice, and which ones should be taken with more caution because a 3D model would be more trustworthy to resolve them.

2. Methods

First, the tested urban configurations are introduced, their link with prototype-scale urban building layouts is discussed and the experimental facility is described (Section 2.1). The considered flooding scenarios are presented in Section 2.2. The 2D and the 3D computational models are detailed (Section 2.3).

2.1. Urban Configurations and Experimental Setup

2.1.1. Urban Configurations

Four geometric configurations were considered. Each of them represents a portion of an idealized urban district with distinct layouts of rectangular prismatic obstacles (Figure 1). In each configuration, three inlet branches and three outlet branches are present. All street intersections have an angle of 90°. The width of all main streets, including the inlet and outlet branches, was constant and equal to 0.2 m.

The four considered urban forms differ by the size and positioning of rectangular obstacles positioned in the central region of the experimental model. As detailed in Figure 1b, they are labeled CE, CO, BD, and Px5. In Configuration CE, the central region is left empty to create a large open space representing a typical square in an urban area. Though in real-world squares, the bottom is generally not flat, it was kept horizontal here for the sake of simplicity. In contrast, Configuration CO involves one large rectangular obstacle covering most of the central region, so that only a network of streets is reproduced, without large open areas. It leads to an urban layout with two four-branch crossroads and two three-branch crossroads, identical to the setup used by Li et al. (2020) and Li, Kitsikoudis, et al. (2021). In Configurations Px5 and BD, six rectangular obstacles of the same size ($l_x = 0.09$ m, $l_y = 0.36$ m, Figure 1) are positioned at different locations to reproduce small streets and relatively large open spaces surrounded by building blocks or located upstream of building blocks. More details on these layouts were presented by Li, Erpicum, et al. (2021) and Li et al. (2022b).

Three of the four tested configurations (CE, CO and Px5) are a subsample of a set of 19 configurations studied by Li, Erpicum, et al. (2021). These 19 configurations were obtained by systematically varying independent parameters controlling the urban building layouts: the number of streets aligned along directions x and y, as well as the width of these streets. The configurations selected here (CE, CO and Px5) were reproduced experimentally, whereas other configurations considered by Li, Erpicum, et al. (2021) were analyzed only by means of computational modeling. Since, the goal of the present research is to assess the performance of 2D and 3D computations against laboratory observations, the set of configurations was limited to those for which laboratory observations are available. The fourth tested configuration (BD) is a variation of Configuration Px5. It was also tested experimentally (Li et al., 2022a).

2.1.2. Link With Prototype-Scale Configurations

The present research was entirely conducted at the laboratory-scale: both the experiments and the computations were performed based on dimensions corresponding to the experimental setup. Therefore, the comparisons presented here between laboratory observations and modeling outcomes are by no means influenced by the choice of a particular scaling procedure. Nonetheless, we provide here an interpretation of the tested urban layouts as a reduced scale representation of real-world configurations. The aim is solely to suggest the plausibility of the tested urban layouts.

In real urban flooding conditions, the horizontal characteristic lengths (e.g., street width) are typically of the order of 10–10^2 m. This is considerably larger than the vertical characteristic dimensions (e.g., flow depth) which range typically between 10^{-1} and 1 m (or 10 m in extreme flood conditions). Therefore, it is common to opt for a geometrically distorted scale model laboratory studies of urban flooding at the level of a network of streets (Arrault et al., 2016; Finaud-Guyot et al., 2018; Güney et al., 2014; Li, Kitsikoudis, et al., 2021; Smith et al., 2016). The vertical scale factor e_V, representing the ratio of the flow depths at protype and laboratory scales, is assigned a larger value than the value of the horizontal scale factor e_H, defined as the ratio of horizontal dimensions at the protype and laboratory scales. Geometric distortion contributes to ensuring a higher Reynolds number in the laboratory experiments and reducing the measurement errors in relative terms (e.g., Li et al., 2020).

Assuming a vertical scale factor $e_V = 5$ and a horizontal scale factor $e_H = 50$ (corresponding to a geometric distortion ratio e_H/e_V of 10), the 0.2 m wide main streets in the configurations described in Subsection 2.1.1 correspond to 10 m wide streets at prototype scale (as encountered in some densely urbanized areas, as reported by Mignot et al., 2006), whereas the 0.1 m flow depth prescribed at the outlets in the experiments (see Section 2.2) represents an inundation depth of 0.5 m at prototype scale. This falls in a range of flow depths frequently encountered in floodplains in case of riverine flooding. This upscaling of the experimentally tested configurations is an example. By adjusting the values of the horizontal and vertical scale factors, our tests may also be regarded as representative of other real-world configurations (Li et al., 2020; Li, Kitsikoudis, et al., 2021).

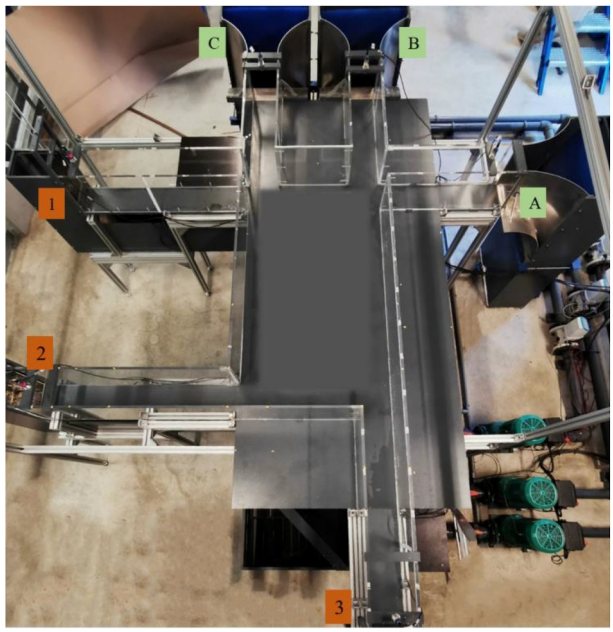

Figure 2. Physical model of the street network, configuration CE. The letters A–C and the numbers 1–3 denote the inlets and the outlets of the physical model, respectively.

Here, since the model geometry and boundary conditions were kept the same in the laboratory experiments and in the computations, the Reynolds number and Froude number remain also unaltered between observations and computations.

2.1.3. Experimental Setup

The experiments were conducted in a physical model at the Laboratory of Engineering Hydraulics at the University of Liege in Belgium (Figure 2). It represents the urban layouts described in Figure 1b. The width of the inlet and outlet channels is 0.2 m, and the height of the transparent outer sidewalls is 0.3 m. In Configurations Px5 and BD, the building blocks placed in the central part of the model are made of smooth Plexiglass plates of 0.15 m in height.

The bottom of the model is horizontal and made of smooth PVC, while the vertical sidewalls are made of Plexiglas. The roughness height of both materials was estimated at $k_s = 5\ 10^{-5}$ m. As discussed by Li et al. (2020) [Section 6.1], this material can mimic various roughness heights at prototype scale depending on the considered scale factors and flood scenarios. If a vertical scale factor in the range of 10–100 is assumed, the corresponding prototype-scale roughness would be between 5×10^{-4} m and 5×10^{-3} m, which seems reasonable to characterize standard materials encountered in urban environments such as asphalt or pavements.

Three independent pipes and pumps were used to supply steady inflow discharge to each inlet branch (labeled A, B and C in Figures 1a and 2). A baffle wall with a honeycomb pattern was used in each inlet branch to reduce swirl and smoothen the incoming flow. In all tests, the inflow discharge was set at the same value in each inlet. Inflow discharges were monitored by electromagnetic flowmeters (SIMENS-MAG 5100W) with an accuracy of 0.5% (full range [0–80] m^3/h).

The flow depth at each of the three outlets (labeled 1, 2 and 3 in Figures 1a and 2) was regulated with adjustable weirs. They were set at the same value at the three outlets.

Nine ultrasonic sensors (Microsonic: Mic+35/IU/TC) were utilized to monitor the water levels at model inlets (green crosses in Figure 1a), model outlets (red crosses in Figure 1a) and in the discharge measurement channels. The measurement accuracy is 1 mm and the sampling rate is 100 Hz. To alleviate the effect of small fluctuations in the recorded signals, they were averaged over an interval of 120 s as described by Li, Erpicum, et al. (2021).

The outflow discharge through each of the three outlets was collected in separate measurement channels (straight horizontal channels, 1.5 m long and 0.2 m wide), each equipped with a 90° triangular sharp-crested weir at their downstream end. The discharges were estimated by employing calibrated rating curves (Li et al., 2022a). The calibration points and the calibrated rating curves for each of the three outlets are displayed in Figures S1a, S1c and S1 in Supporting Information S1. The agreement between the regression and the data points is characterized by a coefficient of determination R^2 exceeding 0.99 in all cases. Figures S1b, S1d and S1f in Supporting Information S1 shows that the relative error between the measured values and the values calculated with the calibrated rating curves remains below 1% when the monitored discharge exceeds 3 $m^3\ h^{-1}$. To enable accurate measurements of outflow discharges below 3 $m^3\ h^{-1}$, such small outflow discharges were measured in the lab by manually monitoring the filling rate of a bucket, so that the measurement uncertainty remains below 1% irrespective of the value of the outflow discharge. More details on this procedure are given by Li et al. (2022a, 2022b). To ensure reproducibility of the results, all measurements were repeated twice as detailed by Li, Erpicum, et al. (2021).

Large scale particle image velocimetry (LSPIV) was used to measure surface velocity. A commercial camera LUMIX-GH4 (resolution of 1,920 × 1,080 pixels, 25 frames per second) positioned 2 m above the bottom of the laboratory model was utilized. The area of interest was covered by combining movies recorded from several viewpoints. This enables minimizing hidden areas and increases the spatial resolution. In regions where movies obtained from several viewpoints overlap, it was possible to show that the velocity estimates from the different movies were consistent, as detailed by Li, Erpicum, et al. (2021) and Li et al. (2022a, 2022b).

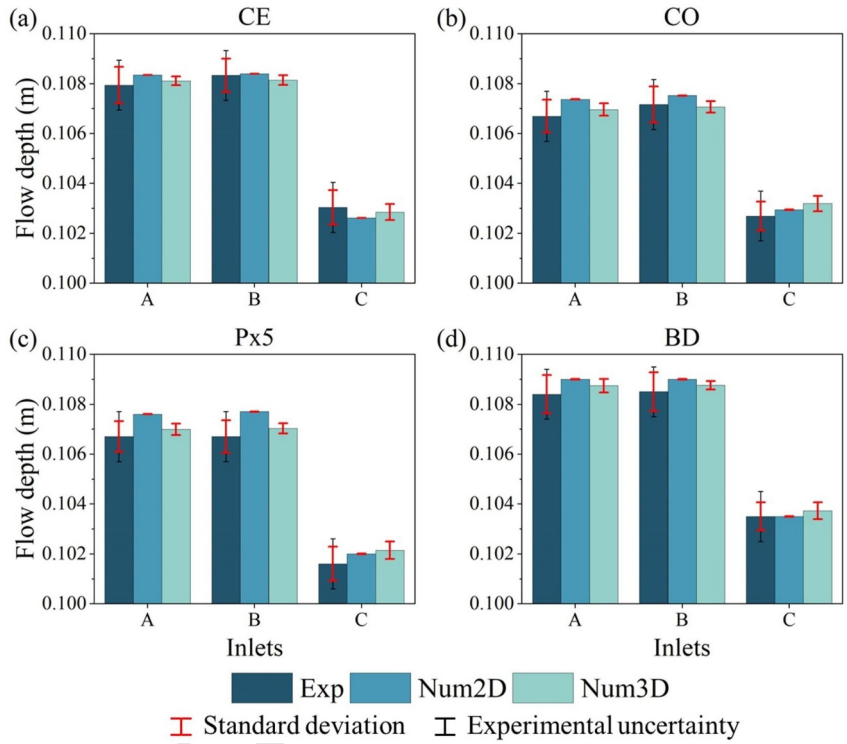

Figure 3. Observed and computed flow depths upstream of each inlet in the four tested urban configurations. Black error bars represent the experimental accuracy (±1 mm), while the red ones reflect the standard deviation of the time series.

Sawdust with a diameter between 1 and 3 mm was selected as seeding material. Its light color contrasting well with the PVC bottom of the model (Figure S2 in Supporting Information S1). The sawdust was injected at the three inlets and captured at each outlet with a basket. Each video was recorded during at least 60 s (i.e., 1,500 images), which was found sufficient to reach convergence of the results (Li, Erpicum, et al., 2021; Li et al., 2022a, 2022b). The recorded sequences were analyzed with the software Fudaa-LSPIV (Le Coz et al., 2014; Zhu and Lipeme Kouyi, 2019). More details about the image processing are provided in Text S1 in Supporting Information.

A direct quantification of the uncertainties affecting LSPIV results is hardly feasible due to the spatial nature of the analysis and the steps involved in the image processing procedure.

2.2. Flooding Scenario

For the four tested urban configurations, identical boundary conditions were prescribed in the computations and in the laboratory experiments. At each outlet, a value of flow depth was prescribed as downstream boundary condition, while the value of the inflow discharge was prescribed as the upstream boundary condition at each inlet.

To simplify the definition of the considered flooding scenario, the flow depth was set at the same value at the three outlets (1, 2 and 3), and the total inflow discharge was evenly distributed between the three inlets (A, B and C). Therefore, a "flooding scenario" is here entirely defined by one value of downstream flow depth (h_0) and one value of inflow discharge in each street (Q_{in}).

To determine the model boundary conditions, we followed a two-step procedure. First, a flooding scenario was defined at prototype scale. Second, the corresponding values of h_0 and Q_{in} were transferred to the model scale using values of e_H and e_V.

At prototype scale, a value of $h_0 = 0.5$ m was considered plausible for urban flooding conditions. Assuming a vertical scale factor $e_V = 5$ (Section 2.1.2) leads to $h_0 = 0.1$ m at the model scale.

In line with Li et al. (2020), Li, Erpicum, et al. (2021) and Li, Kitsikoudis, et al. (2021), a characteristic Froude number F (−) was introduced to determine a plausible inflow discharge. It is defined based solely on input data, that is, the flow depth h_0 (m), the inflow discharge Q_{in} (m^3/s) and the width b (m) of the main streets:

$$\mathrm{F} = \frac{Q_{in}}{b\, h_0 \sqrt{g h_0}} \tag{1}$$

Note that this definition of the Froude number F is introduced here only for defining the flooding scenario, observed and computed local values of the Froude number in the considered urban configurations considerably deviate from the value of parameter F. Local values of the Froude number typically exceed unity in the vena contracta downstream of the street intersections, as displayed in the maps of local Froude numbers computed by Li et al. (2020) (see their Figure 3).

By setting a value for F, the inflow discharge Q_{in} at each inlet can be determined from Equation 1. Here, the flow was assumed relatively slow, with a characteristic Froude number F of 0.2, consistent with typical values observed in floodplains of lowland rivers. This leads to a value of Q_{in} = 14.26 m^3/hr at model scale (corresponding to 2.2 m³/s at prototype scale), and an inlet Reynolds number at model scale equal to 4×10^4.

2.3. Computational Models

2.3.1. 2D Model

The academic modeling system WOLF developed at the University of Liège was used in this study. It solves the 2D shallow-water equations with a finite volume technique on a Cartesian grid. These equations correspond to the Reynolds-averaged Navier-Stokes equations along the x and y directions, integrated over the water depth. Considering a horizontal bottom, they write as follows (Camnasio et al., 2014; Erpicum et al., 2009):

$$\frac{\partial hu}{\partial t} + \frac{\partial hu^2}{\partial x} + \frac{\partial huv}{\partial y} + \frac{\partial}{\partial x}\left(\frac{gh^2}{2}\right) = \underbrace{\frac{\tau_{bx}}{\rho}}_{①} + \underbrace{\frac{1}{\rho}\frac{\partial h\tau_{xx}}{\partial x} + \frac{1}{\rho}\frac{\partial h\tau_{xy}}{\partial y}}_{②} \tag{2}$$

$$\frac{\partial hv}{\partial t} + \frac{\partial huv}{\partial x} + \frac{\partial hv^2}{\partial y} + \frac{\partial}{\partial y}\left(\frac{gh^2}{2}\right) = \underbrace{\frac{\tau_{by}}{\rho}}_{①} + \underbrace{\frac{1}{\rho}\frac{\partial h\tau_{xy}}{\partial x} + \frac{1}{\rho}\frac{\partial h\tau_{yy}}{\partial y}}_{②}, \tag{3}$$

with t the time (s), u and v the depth-averaged velocity components (m/s) along the horizontal directions x and y (m), h the flow depth (m), ρ the water density (kg/m^3) and g the gravity acceleration (m/s^2). The derivatives of the depth-averaged viscous and turbulent stresses τ_{xx}, τ_{xy} and τ_{yy} (N/m^2) are expressed using Boussinesq's assumption. The eddy viscosity was evaluated based on a depth-averaged k-ε turbulence model (Camnasio et al., 2014; Erpicum et al., 2009). The parameters involved in the k-ε turbulence model were kept at their default values and they were not recalibrated here. This setting of the model was successfully used to reproduce flow features in urban flooding studies either based on the same experimental setup as here (Li, Erpicum, et al., 2021, Li, Kitsikoudis, et al., 2021), or with different setups (Arrault et al., 2016; Dewals et al., 2023).

The x- and y-components of the bottom shear stress τ_{bx} and τ_{by} (N/m^2), are estimated using the Darcy-Weisbach formulation with Colebrook-White equation. The roughness height (k_s) of the smooth PVC plates constituting the experimental setup is estimated at 5×10^{-5} m. This particular value has little influence on the computational results, as demonstrated by Li, Erpicum, et al. (2021) for the same computational model and experimental facility as considered here.

More details on the setting of this 2D model were presented by Li et al. (2020), Li, Erpicum, et al. (2021) and Li, Kitsikoudis, et al. (2021). The ability of this model to simulate complex turbulent flow as well as urban flooding was partly assessed in previous studies (Arrault et al., 2016; Bruwier et al., 2017). The computational domain was meshed with ∼[8.2–10.6] × 10^4 square cells. A mesh sensitivity analysis was detailed by Li et al. (2020).

At the downstream boundaries of the computational domain (Outlets 1, 2 and 3 in Figure 1a), a constant flow depth of 0.1 m was prescribed as a weak boundary condition on the cell interfaces. At the inlet boundaries (Inlets

Table 1
Main Characteristic of the 3D Computational Domain

Implementation	OpenFOAM
Solver	interFOAM
Turbulence model	RANS k-ω SST
Wall treatment	Standard wall function
Discretization schemes:	
Gradients	Second-order least squares
Divergence	Second-order upwind
Turbulent kinetic energy	Second-order upwind
Time derivative	First-order implicit
Multiphase model	VOF
Interface capturing scheme	MULES scheme
Pressure-velocity coupling	PISO scheme
Boundary conditions	
Inlet	flowRateInletVelocity $3.962 \lozenge 10^{-3}$ m/s (14.26 m^3/hr)
Outlet	pressureInletOutletVelocity
Atmosphere	pressureInletOutletVelocity

A, B and C in Figure 1a), a constant unit discharge of 0.02 m^2/s in the direction normal to the boundary was prescribed as a weak boundary condition, corresponding to an inflow discharge of 14.26 m^3/hr in each of the three inlets. The unit discharge parallel to the inlet boundaries was set to zero. At cell interfaces corresponding to solid walls, the component of the unit discharge normal to the wall was set to zero. The discretization of the turbulent diffusion terms and turbulence quantities at the boundaries was kept the same as described in Erpicum et al. (2009) and Camnasio et al. (2014).

In the configurations tested here, the 2D computations generally converge toward quasi-periodic flow fields, with small oscillations in the computed flow parameters. This was discussed in detail by Li et al. (2020) and primarily attributed to time-variations of flow separation zones downstream of street intersections. The computations properly capture these oscillations since their characteristic time is substantially longer than the numerical time step. The scope of the present study focuses on the time-averaged quantities. Therefore, the simulation results were time-averaged following the same procedure as described by Li et al. (2020).

The computational time necessary for the 2D simulations to reach a steady state varied with the studied geometric configuration and the initial conditions. In most cases, it took about an hour on a standard desktop (4-core processor Intel i7-6700K, 4 GHz).

2.3.2. 3D Model

For simulating in 3D the flow in the experimental setup, the incompressible Reynolds-Averaged Navier-Stokes (RANS) equations were solved, together with a turbulent closure model based on a Boussinesq-type eddy viscosity assumption:

$$\nabla \cdot U = 0 \tag{4}$$

$$\frac{\partial U}{\partial t} + \nabla \cdot (UU) = -\nabla P + \nabla((\nu + \nu_t)\nabla U) \tag{5}$$

with U the velocity vector (in 3D) (m/s), P the pressure (Pa), ν the fluid kinematic viscosity (m^2/s) and ν_t the eddy viscosity (m^2/s). These equations were solved with the open-source software OpenFOAM (v. 6.0). The adopted solver is interFoam and the k-ω SST turbulence closure model was used; The latter was chosen because it was repeatedly used and validated for a broad range of engineering applications (Versteeg and Malalasekera, 2007).

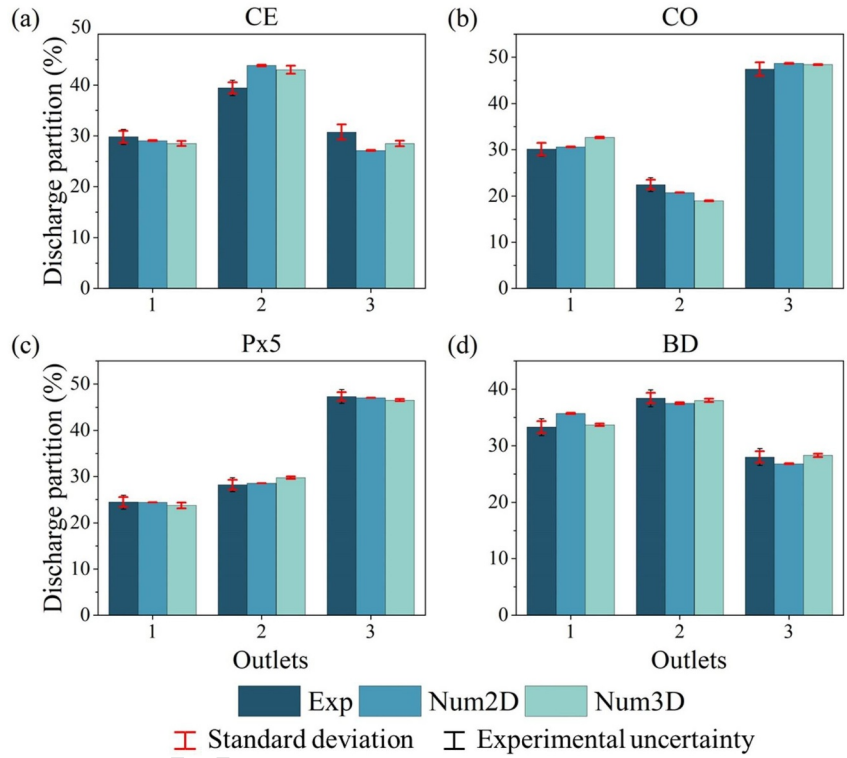

Figure 4. Observed and computed discharge partition at each outlet for the four tested configurations. Black error bars represent the experimental accuracy, while the red ones reflect the standard deviation of the time series (i.e., the variability in time of the results).

The free surface was captured thanks to the volume of fluid (VOF) method introduced by Hirt and Nichols (1981). This method is computationally efficient, and it was commonly used and extensively validated. Detailed information about this method can be found in Versteeg and Malalasekera (2007). A CFL restriction of 2 was imposed which leads to an adjustable time step of the order of 0.002s. More characteristics of the model are summarized in Table 1. The simulations were run on a structured mesh composed of [2.4–3.2] million cells built with the *blockMesh* utility with uniform mesh size of 0.005 m, mesh refinement near the solid wall was not considered as the wall function was applied.

At the three model inlets, a constant flowrate of 3.962×10^{-3} m^3/s (14.26 m^3/hr) was imposed with the feature "*flowRateInletVelocity*" (aligned with the inlet sidewalls, Figure S3 in Supporting Information S1); "*pressureInletOutletVelocitsy*" was applied at each model outlets and the atmosphere.

Although the model boundary conditions are steady, the simulated results (i.e., flow depths, discharge, velocities) show some fluctuations similarly to the case of the 2D model. Therefore, the computational results were averaged over a period of about 20 s. As shown in Figure S4 in Supporting Information S1, this results in smoothing out minor fluctuations, which remain small compared to the quantities of interest. A similar approach was used in several previous studies, such as in Torres et al. (2022). The 3D simulations were performed on 48-core computer and take about 6 hr to simulate 120 s of physical time, which is sufficient for reaching a steady state.

3. Results and Discussion

Section 3.1 and 3.2 compare, respectively, the computed flow depths at the street inlets and the partition of outflow discharge against experimental observations. These variables are considered as integral quantities reflecting the cumulative effect of flow processes and losses across the urban district. In Section 3.3, similarities and differences between computed and observed, depth-averaged and surface velocity fields are discussed. Three-dimensional flow features revealed by the computations are presented in Section 3.4. Table S1 in Supporting Information S1 summarizes the main findings.

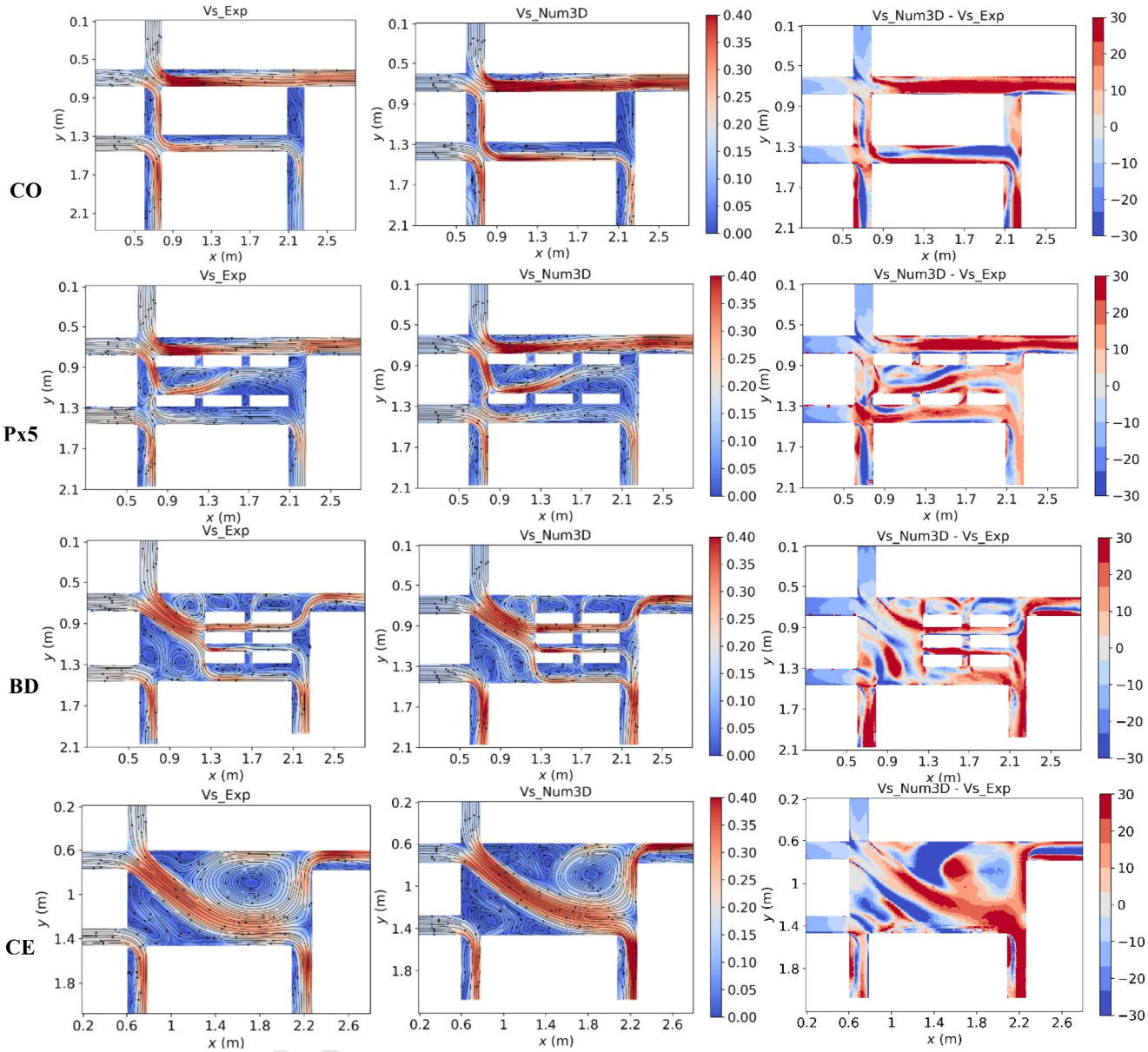

Figure 5. Surface velocity field (m/s) in the four tested urban configurations: LSPIV measurements ("vs._Exp"), surface velocity computed by the 3D model ("Vs_Num3D"), and difference between these two quantities (%). The difference between the computed and measured velocities is normalized by a characteristic velocity of 0.2 m/s.

3.1. Inlet Flow Depths

The observed and computed values of flow depth at each street inlet (green crosses in Figure 1a) are displayed in Figure 3 for the four tested configurations (values are detailed in Table S2 in Supporting Information S1). Irrespective of the urban configuration, observed flow depths at inlets A and B are about 5% (4–5 mm) higher than those at inlet C. Although this difference is limited in magnitude, it is accurately captured by both the 2D and the 3D models. In all cases, the difference in-between the models as well as between computations and observations does not exceed 1 mm, which corresponds to the accuracy of experimental measurements (represented by black error bars of ±1 mm in Figure 3). Time variability of the results (red error bars in Figure 3) is lower than the experimental uncertainty. Hence, as regards the prediction of inlet flow depths in the tested configurations, we

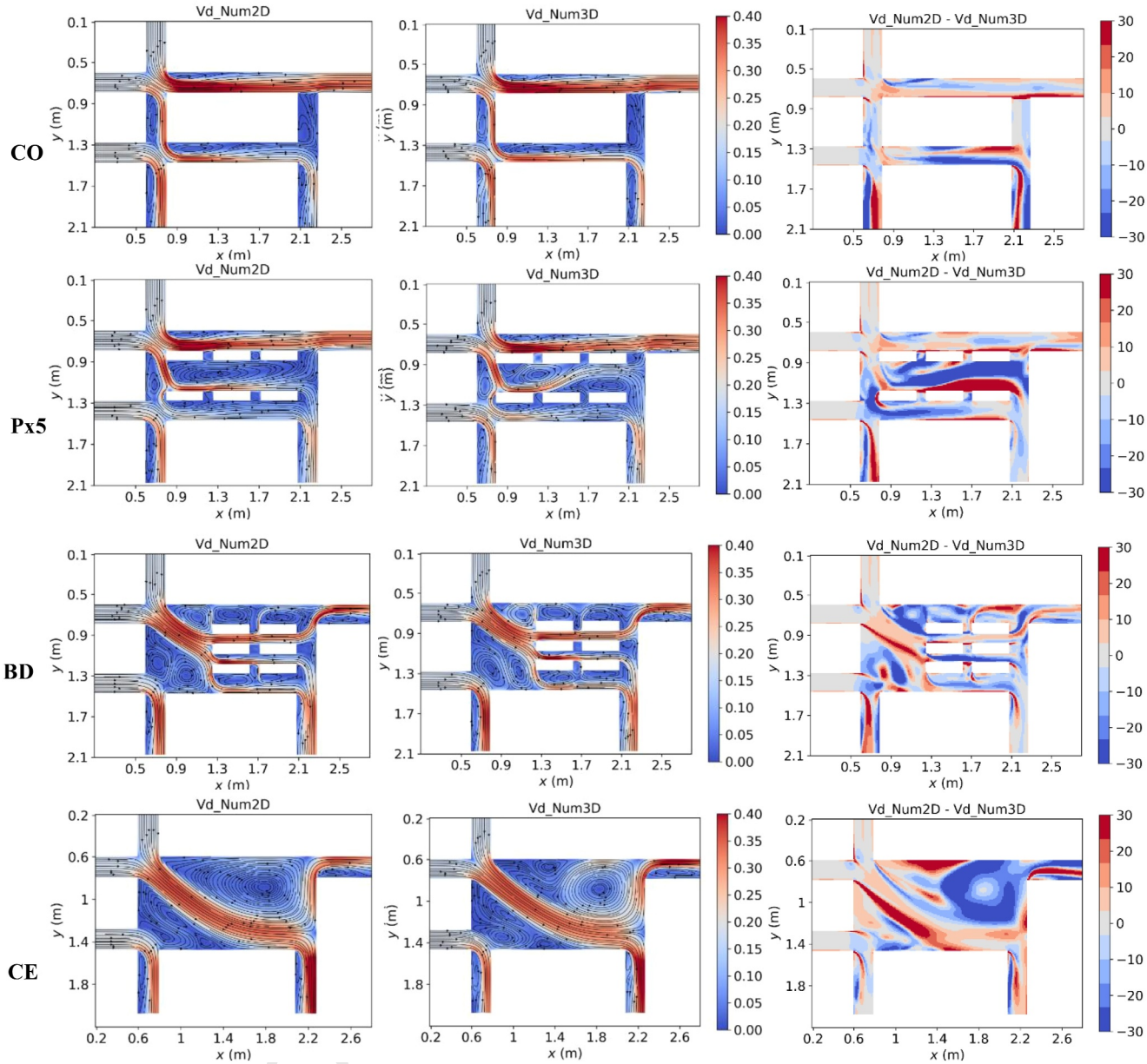

Figure 6. Depth-averaged velocity field (m/s) in the four tested urban configurations: computed depth-averaged velocity by the 2D model ("Vd_Num2D") and by the 3D model ("Vd_Num3D"), as well as difference between these two quantities (%). The difference is normalized by a characteristic velocity of 0.2 m/s.

find no significant deviation between the computations and the observations, nor between the two computational models.

3.2. Outflow Discharge Distribution

3.2.1. Observations

While the upstream flow depths appear not affected by the layout of the urban block, the discharge partition in-between the street outlets varies substantially with the geometric configuration (Figure 4, values are detailed in Table S3 in Supporting Information S1).

- The discharge distribution between the three outlets is relatively balanced in the case of Configuration CE. The discharge share at each specific outlet does not deviate from one third by more than two to six percent-points.

- In Configuration CO, about half of the total injected discharges ends up in Outlet 3. Outlet 1, which is close to Inlet C, receives 30% and Outlet 2 only 20%. This discharge distribution favoring Outlet 3 relates to the split of discharge induced by the north-west corner of the urban block, which diverts a higher share of the inflow discharge toward Street B-3 (i.e., from Inlet B to Outlet 3). This is consistent with the velocity fields represented in Figure 6 hereafter.
- In Configuration Px5, the discharge fraction exiting through Outlet 3 is the same as in Configuration CO (47%). Outlet 2 receives 28% of discharge and Outlet 1 only 24%. Similarly to Configuration CO, the relatively high share of discharge conveyed toward Outlet 3 is linked to the effect of the obstacle positioned at the north-west corner of the central area.
- In Configuration BD, Outlet 1 attracts about one third of the total discharge, while Outlet 2 attracts almost 40% and Outlet 3 less than 30%. This may be attributed to the predominantly oblique flow across the urban layout, which is oriented from north-west toward south-east (close to Outlet 2), as shown in Figure 6. The 3D model accurately captures this pattern, with differences between computed and observed values remaining below one percent-point. The 2D model also performs well, with differences compared to experiments of maximum two percent-points.

3.2.2. 2D Model Versus 3D Model

Differences between the distributions of outflow discharges predicted by the 2D and the 3D models remain small. Indeed, the computed fractions of outflow discharge from the two numerical models differ generally by no more than one percent-point, which is comparable to the estimated accuracy of outflow discharge measurements at each outlet, that is, 1% according to Li et al. (2022b). Only at Outlets 1 and 2 in Configuration CO and Outlet 1 in Configuration BD the difference between the 2D and the 3D models reaches two percent-points. Still, this remains below the overall experimental mass balance error which is of the order of 2.5% of the total injected discharge Li et al. (2022b).

3.2.3. Computations Versus Observations

Both the 2D and 3D models provide good estimates of the outflow discharge distribution.

- In Configurations Px5 and BD, the differences between computed and observed outflow discharge fractions remains below the overall experimental mass balance error of 2.5% of the total injected discharge Li et al. (2022b).
- In Configuration CO, deviations between 2D computations and observations also do not exceed two percent-points, while the 3D model underpredicts by about four percent-points the discharge fraction at Outlet 2 and it overpredicts by nearly three percent-points at Outlet 1 and by one percent-point at Outlet 3.
- In Configuration CE, both models overpredict by about four percent-points the outflow discharge fraction at Outlet 2, and underpredict by two (3D model) to nearly four (2D model) percent-points at Outlet 3. This may be attributed to a mismatch between the characteristics (size and flow velocity) of the large horizontal recirculations computed by the models and experimentally observed, as detailed in Section 3.3 and Figure 5 hereafter.

From the comparison of the outflow discharge distributions, it is impossible to state that one of the two computational models overperforms compared to the other one. Indeed, most deviations between computations and observations are below or close to the experimental uncertainties, and the differences between the predictions of the two models are systematically lower than the experimental uncertainties. Moreover, in some configurations, the 2D model performs slightly better than the 3D model (Configurations CO and Px5), whereas in others the 3D model outcomes are closer to the observations (Configurations BD and, to a lesser extent, CE). The latter result suggests that the 3D model seems to better predict the outflow discharge distribution in urban layouts involving relatively large open spaces (such as CE and western part of BD), while the 2D model is accurate when the flow is well guided by the streets layouts, such as in Configuration CO.

3.3. Surface and Depth-Averaged Flow Velocity

Figure 5 displays the surface velocity field measured in the experiments (labeled "Vs_Exp") and computed by the 3D model (labeled "Vs_Num3D"), as well as the differences between these two quantities. The differences are normalized by a reference velocity (0.2 m/s), defined as the mean velocity which would be observed at the street

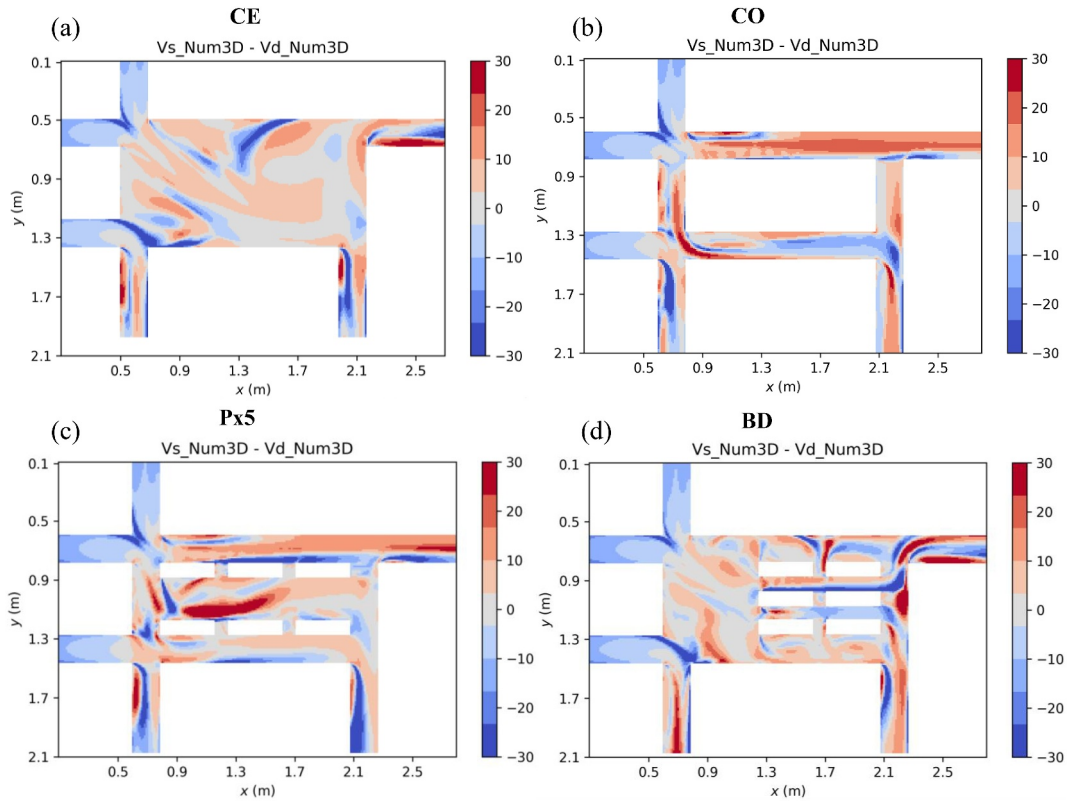

Figure 7. Differences between surface (labeled "Vs_Num3D") and depth-averaged (labeled "Vd_Num3D") velocities computed by the 3D model (%). The difference is normalized by a characteristic velocity of 0.2 m/s.

outlets in the hypothetical case of an outflow discharge evenly distributed between the three outlets. Figure 6 represents the depth-averaged velocity computed by the 2D and the 3D models (labeled "Vd_Num2D" and "Vd_Num3D", respectively) and the difference between these two quantities, also normalized by a reference value (0.2 m/s). The depth-averaged velocity was evaluated from the 3D model results by averaging the velocity fields computed at seven distinct elevations ($z = 1$ cm, 2 cm, 3 cm, 5 cm, 7 cm, 9 cm and at the surface above the flat horizontal bottom) based on the trapezoidal rule. Examples of velocity profiles are displayed in Figures S8 and S9 in Supporting Information S1. Differences between computed surface and depth-averaged velocities are displayed in Figure 7 (see also Figure S7 in Supporting Information S1).

A qualitative appraisal of the velocity patterns, based on visual inspection of Figures 5 and 6, reveals a good match between the computed and observed surface velocity fields, as well as between depth-averaged velocity fields computed in 2D and in 3D. Nonetheless, the agreement between the velocity fields varies slightly with the considered region of the domain, that is, whether in channelized areas (streets, inlet branches) or in open areas (i.e., central part of Configurations CE and Px5, and western part of Configuration BD).

3.3.1. Inlet Branches and Streets

In the inlet branches, the 3D model systematically underestimates the surface velocities by about 10%, irrespective of the urban configuration (Figure 5). In contrast, the depth-averaged velocities computed by the 2D and the 3D models are consistent in all inlet branches (Figure 6). From a mass balance perspective, the latter result is consistent with the accurate estimation of inlet flow depths by the two models (Section 3.1), as well as with the computed depth-averaged velocity exceeding the computed surface velocity by about 10% in the inlet branches (Figure 7).

In the contraction zones located immediately downstream of street intersections (e.g., $x \sim 1.2$ m in Configurations CO and Px5), the surface velocity fields computed with the 3D model agree well with the experimental observations. In contrast, more discrepancies are found between the computed and measured surface velocities

Table 2
Locations of Crosswise Sections for the Four Configurations, Red-Dashed Lines in Figure 1b

Configurations	Sections	x (m)	y (m)
CE	CE-1, … , CE-4	1.2, 1.4, 1.6, 1.8	[0.6–1.48]
CO	CO-1, … , CO-5	0.95, 1.15, 1.2, 1.4, 1.6	[0.6–0.8]
Px5	Px5-1, … , Px5-5	1, 1.2, 1.45, 1.65, 1.9	[0.6–0.8]; [0.89–1]
BD	BD-1, … , BD-5	0.8, 0.95, 1, 1.1, 1.2	[0.6–1.48]

downstream of the *vena contracta*, such as in the west-east street B3 (see blue-shaded areas in Figure 1b) for $x > 1.2$ m, in Configurations CO and Px5. The 3D model overestimates surface velocity by up to 30% of the reference velocity (Figure 5). In the same urban configurations, despite differences between computed surface and depth-averaged velocities (Figure 7), the depth-averaged velocities computed by the 2D and by the 3D model agree very well both in the *vena contracta* and also further downstream, except close to the sidewalls. This is clearly visible along street B3 in Configurations CO and Px5.

3.3.2. Open Areas

The orientation and shape of the main surface flow jets visible in Configurations CE, Px5, and BD are remarkably well captured by the 3D model (Figure 5). Nonetheless, in Configuration CE, the surface flow velocity computed by the 3D model at the end of the main jet (close to Outlet 2) is overestimated by up to 30% (of the reference velocity) compared to the experimental observations. The shape of the main jet predicted by the 2D model in the middle part of Configuration Px5 differs from the predictions of the 3D model (Figure 6). Indeed, the flow jet computed in 3D reattaches first against the obstacles located in the southern part of the central area, and at mid-length, it reattaches to the obstacles located in the northern part. This behavior is visible both in the surface velocity (Figure 5) and in the depth-averaged velocity (Figure 6). In the 2D simulation, the jet reattaches only along southern obstacles. This alters considerably the pattern of flow recirculations. According to the 3D computations, the region in the middle of urban layout Px5 is characterized by substantial differences (of the order of 30% of the reference velocity) between surface and depth-averaged velocities (Figure 7), as also shown in Figure 11 hereafter.

The relative sizes and shape of experimentally observed surface flow recirculations in large open areas are generally well reproduced by the 3D computations (Figure 5). For instance, in Configurations CE, the centroid of the main surface flow recirculation observed experimentally and simulated by the 3D model are both positioned close to the point of coordinates $(x, y) \approx (1.8\text{ m}, 0.9\text{ m})$ (see also Figure S2 in Supporting Information S1). Still, some discrepancies remain, such as in the central area in Configuration CE and in the western part of Configuration BD.

In Configuration CE, the size of the main surface recirculation is larger in the experimental observations than in the 3D simulation (Figure 5). Surprisingly, the extent of the main recirculation in the 2D modeling results is closer to the experimentally observed one based on surface velocity (Figure 6); but the velocity magnitude in the recirculation is substantially smaller in the 2D results than in the experimental data and in the 3D results. A similar difference in velocity magnitude is found for the recirculation located close to Inlets A and B in Configuration BD.

In the western part of Configuration BD, the results of the two models also show small differences: the shapes of the recirculation zones computed by the 3D model are more elongated than those computed by the 2D model (Figure 6).

3.4. 3D Flow Features

3.4.1. Regions Downstream of Street Intersections

Examining the results of the 3D model provides valuable information on the flow structure over the flow depth, and hence it hints at regions where a 2D flow model is more or less likely to deliver accurate predictions. Table 2 lists the locations of the cross sections whose iso-velocities (component in the direction normal to the cross-

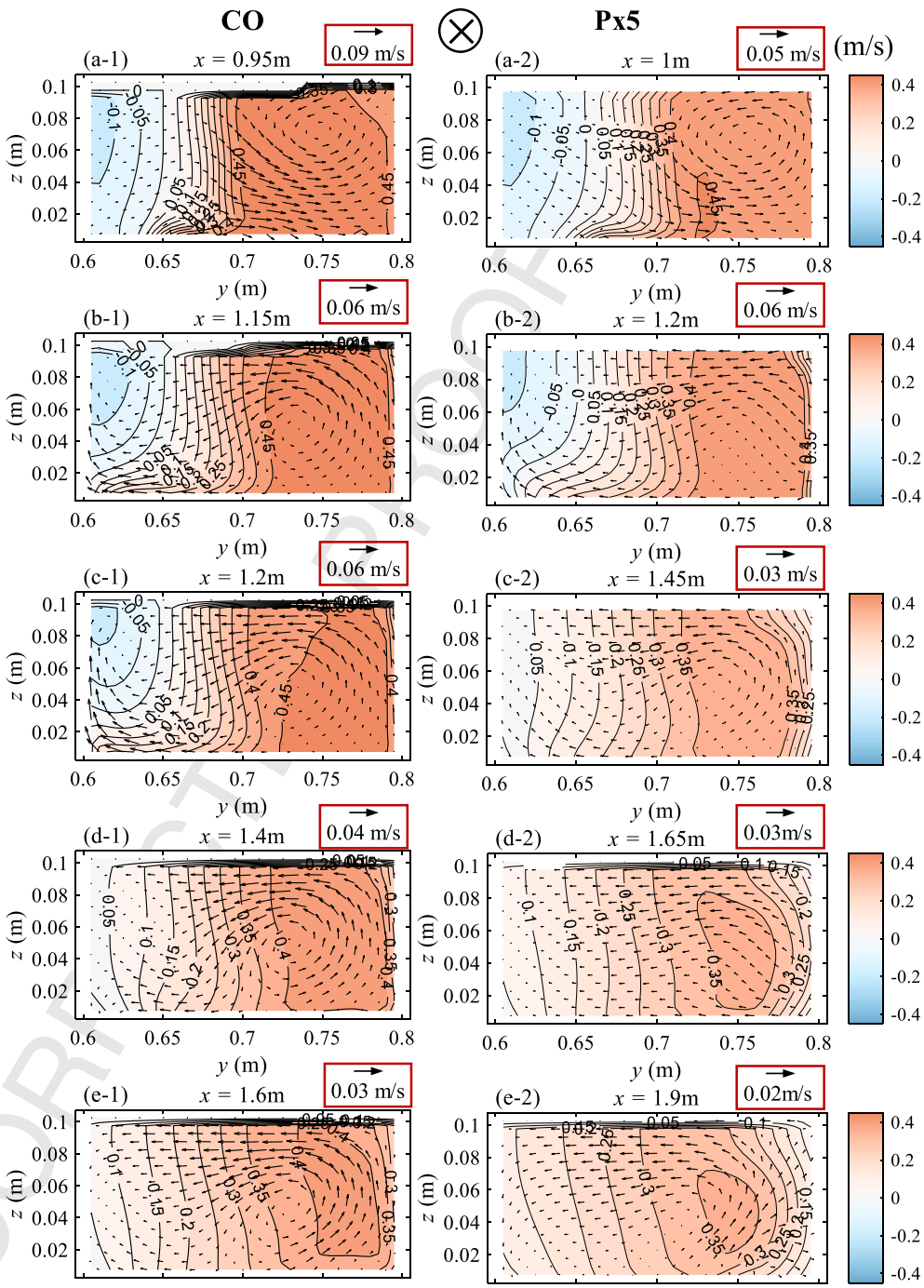

Figure 8. Cross-section view of computed iso-velocity contours (velocity component normal to the cross-section) and secondary currents downstream of a street intersection in Configurations CO and Px5 (cross-sections displayed by red segments in Figure 1b, and defined in Table 1). The value in the red rectangle above each subfigure represents the scale of the arrows).

section) are exhibited hereafter, the positioning of the selected cross-sections is also shown by red segments in Figure 1b. The cross-sections displayed were selected based on the flow pattern of each configuration. We first focus on Configurations CO and Px5 to investigate 3D flow structures downstream of street intersections.

Figure 8 shows contours of iso-velocity (along x direction) in five cross sections along Street B3 (at $x = 0.95$, 1.15, 1.2, 1.4, 1.6 m for Configuration CO and $x = 1$, 1.2, 1.45, 1.65, 1.9 m for Configuration Px5), together with the

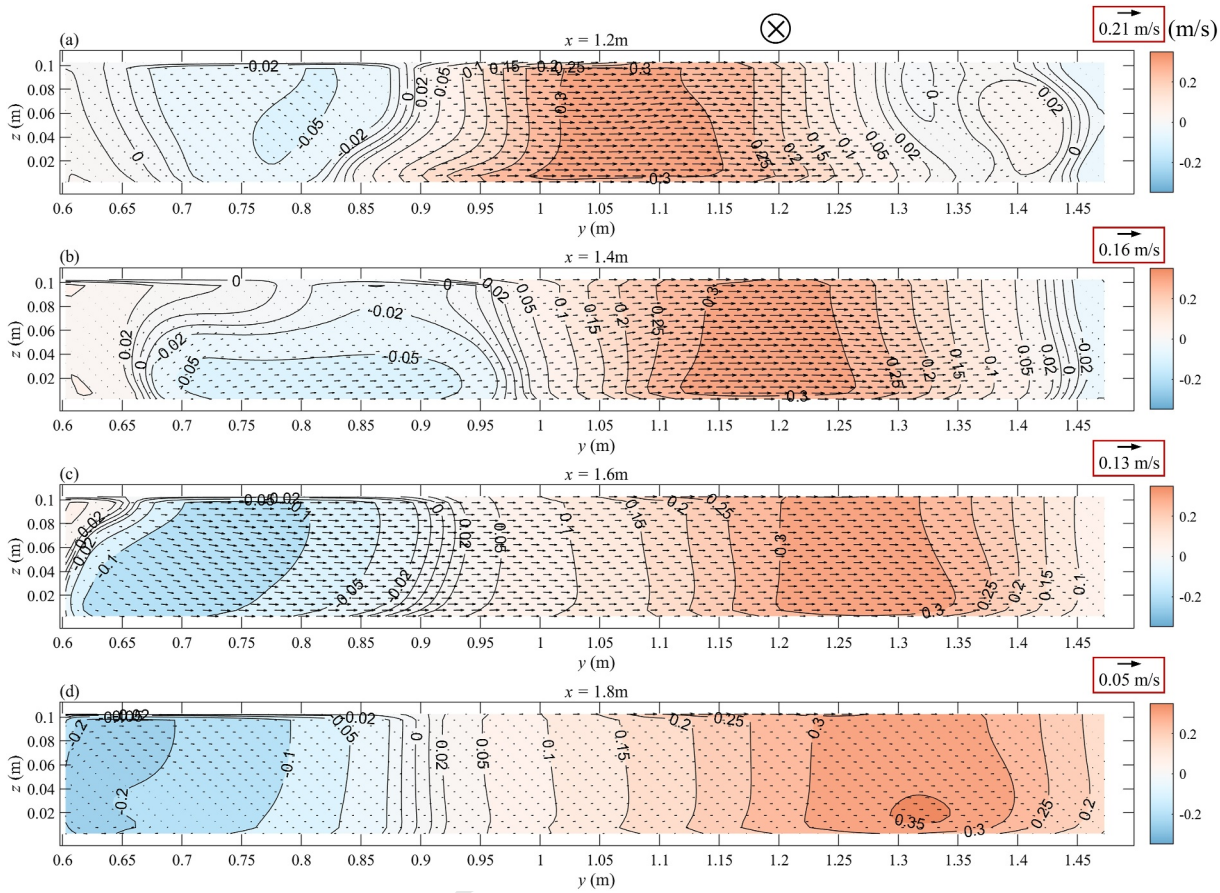

Figure 9. Cross-section view of computed iso-velocity contours (velocity component normal to the cross-section) and secondary currents in four cross sections (displayed by red segments in Figure 1b and defined in Table 1) in Configuration CE.

velocity components in the cross-section (looking from upstream to downstream). Consistently with Figures 5 and 6, the main horizontal recirculation zone and the *vena contracta* are visible, respectively, on the left side and on the right side of the cross sections displayed in Figure 8.

The separation between the *vena contracta* and the main horizontal recirculation zone is characterized a steep velocity gradient along the transverse direction y (Figures 8a-1–8c-1; Figures 8a-2 and 8b-2). This pattern extends almost uniformly over most of the flow depth, except over the lowermost 20% of the flow layer, where the zone of separation is deviated toward the left sidewall. On the side of the *vena* contracta, the velocity profile remains uniform over the flow depth. Further downstream ($x > \sim 1.4$ m), the transverse velocity gradient is considerably reduced, and the distribution of flow velocity normal to the cross-section becomes almost uniform over the flow depth (Figures 8d and 8e).

In most cases, the region of minimum flow velocity normal to the cross-section (light area in Figure 8) extends almost uniformly from the surface to the bottom of the flow layer. Only in the range $x \sim 1.10$–1.20 m (Figures 8b-1, 8c-1 and 8b-2), this region is restricted to the upper half of the flow layer, highlighting substantial deviations from a uniform flow velocity distribution along the vertical direction.

Figure 8 also reveals the presence of secondary currents, rotating counterclockwise. The center of the helicoidal flow is gradually shifted along the streamwise direction, from a position close to the upper right corner of the cross-section (Figures 8a-1 and 8a-2) toward a more centrally located position with $x \approx 0.73$ m and $y \approx 0.04$ m (Figures 8e-1 and 8e-2). Such secondary currents are consistent with previous experimental findings by Yuan et al. (2018) as well as outcomes of 3D computations by Luo et al. (2018) and Chen et al. (2017), who also highlighted similar counter-clockwise helicoidal motion downstream of a junction. In both configurations, the intensity of the secondary currents tends to decrease along the main flow directions.

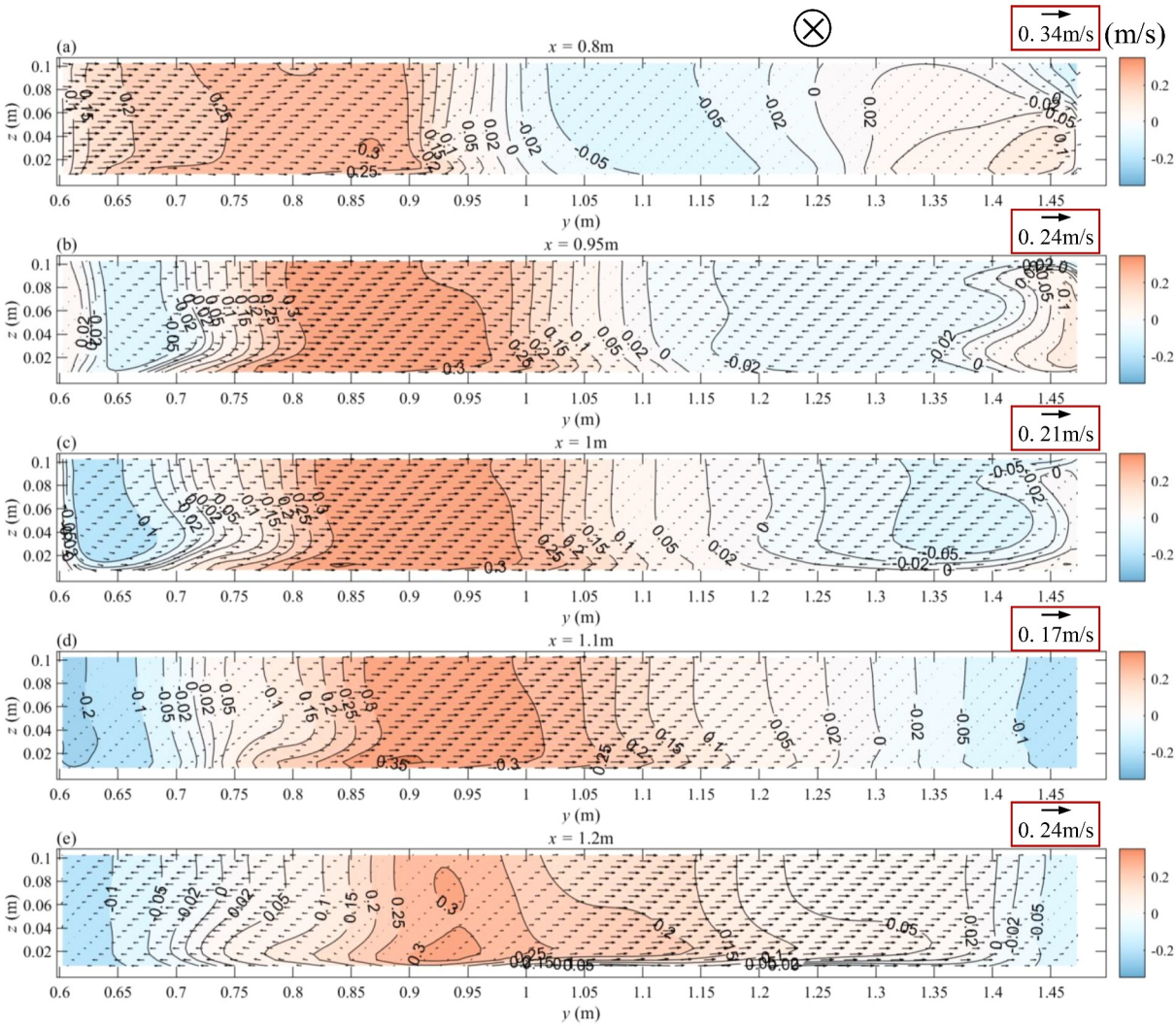

Figure 10. Cross-section view of computed iso-velocity contours (velocity component normal to the cross-section) and secondary currents in four cross sections (displayed by red segments in Figure 1b and defined in Table 1) in Configuration BD.

3.4.2. Open Spaces

Figures 9–11 display a cross-sectional view of computed iso-values of the velocity component normal to the cross-sections, as well as secondary currents in Configurations CE, BD and Px5, respectively. In Configurations CE (Figure 9) and BD (Figure 10), the flow jet is gradually shifted toward the right side of the cross-sections (as x is increased), consistently with Figures 5 and 6. Like in Configuration CO, the boundaries between the main jet and the horizontal recirculation zones are characterized by steep velocity gradients, which are way stronger in the more upstream parts of the jet (Figures 9a, 9b; Figures 10a, 10b) and they become milder further downstream (Figures 9c, 9d; Figures 10c–10e). The shear regions between the jet and the nearby recirculating zones mostly shows a uniform profile over the flow depth, except in the close vicinity of the bottom (Figures 9a and 10a–d). Also in the main jet, the velocity profile remains generally uniform over the flow depth, especially in Configuration BD (Figures 10b–10d), while only in its most upstream part, the jet appears more widely spread close to the bottom. At its downstream end, the jet in Configuration CE also shows a more unevenly distributed pattern over the flow depth (Figure 9d).

In Figures 9 and 10, several regions of quasi zero-velocity can be identified. Their positioning corresponds to the center of horizontal flow recirculations (Figures 5 and 6). In many cases, these quasi-null velocity regions extend uniformly from the surface to the bottom of the flow layer. An exception is represented in Figure 9b, which shows

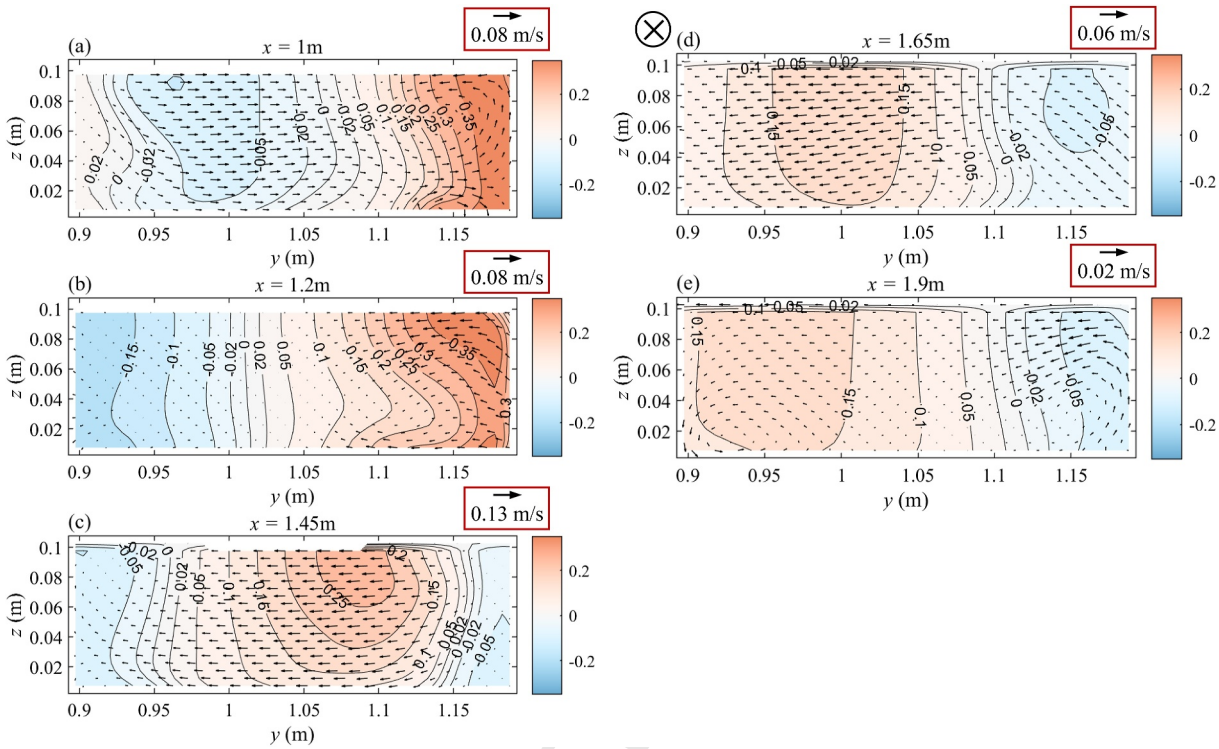

Figure 11. Cross-section view of computed iso-velocity contours (velocity component normal to the cross-section) and secondary currents in four cross sections (displayed by red segments in Figure 1b and defined in Table 1) in Configuration Px5.

a current close to the bottom while the velocity in the upper part of the flow layer is close to zero (Figure 9b). In Figure 9d, the uniform distribution over the flow depth of the quasi-zero velocity region around (x, y) ~ (1.8 m, 0.9 m) is clearly visible, and it was tested experimentally. A tracer with slight negative buoyancy (saturated sawdust) was injected in this area, and it was observed to deposit on the bottom exactly at the same position as the center of the horizontal surface recirculation captured in our LSPIV measurements (Figure S2 in Supporting Information S1), suggesting a good match between the positioning of the quasi-zero velocity region at the surface and close to the bottom. Nevertheless, more detailed velocity measurements are needed to confirm the validity of the computed flow 3D structures.

The shape of the main jet in the middle open space in Configuration Px5 differs from the jets in Configurations CE and BD as it is embedded in-between two rows of rectangular obstacles. As shown by the iso-velocity contours in Figure 11, the jet shifts from the right side to the left side of the cross-sections as x is increased, and the flow velocity in the jet is gradually reduced so that transverse velocity gradients also decreases with increasing values of x. Complex flow velocity patterns develop over the flow depth, with a jet concentrated close to the free surface for x ~ 1.45 m (Figure 11c) and three-dimensional recirculations (Figures 11a–11d). In the cross-section positioned at x = 1.45 m (Figure 11c), the velocity close to the free surface in the jet area is about twice higher than the velocity near the bottom.

Secondary currents are less visible in the open spaces in Configurations CE (Figure 9) and BD (Figure 10) than they are in Configurations CO and Px5 (Figure 8). This may be attributed to a considerable difference in flow aspect ratios (i.e., depth to width ratio). Indeed, in Street B3 in Configurations CO and Px5 (Figure 8), the flow aspect ratio is close to 0.5 (flow depth ~ 0.1 m and street width = 0.2 m), whereas the flow aspect ratio in open spaces in Configuration BD and CE (Figures 9 and 10) is of the order of 0.1 (flow depth ~ 0.1 m, flow width ~ 0.9 m).

Note that an aspect ratio of 0.5 is not common in real-world urban flooding, except for extreme flooding in a network of narrow streets (e.g., historical center of some European cities, as analyzed by Mignot et al., 2006). The high aspect ratio obtained in the experiments conducted here results partly from the geometrical distortion of the

scale model (i.e., lower scale factor along the vertical direction than horizontally). Li, Erpicum, et al. (2021) analyzed the influence of upscaling from model scale to prototype scale, hence also reducing the flow aspect ratio (from about 0.5 to 0.05). Based on their 2D computations, they revealed that this change in aspect ratio has little influence on the upstream flow depths and outflow discharge partition (e.g., 1% point difference). However, the influence of the aspect ratio on 3D flow structures in urban flooding remains a question deserving further experimental research.

Nonetheless, the 3D computational results highlight the complexity of the flow vertical structure in open spaces in urban configurations, which makes the representation of some features of these flow fields particularly challenging with a 2D depth-averaged model, as the jet trajectory in the horizontal plane and the horizontal recirculations are certainly influenced by the flow vertical structure.

3.5. Main Limitations and Research Needs

Though the considered experimental setting was selected to represent a variety of urban layouts (three- and four-branch crossroads, open spaces), they may not be representative of more complex real-world urban areas (Dottori et al., 2013). Therefore, the analysis of real-world urban flood data (e.g., Paquier et al. (2020)) would be valuable to make the conclusions of the present study more robust. One particular aspect of interest is how changes in the flow aspect ratio and the relative roughness height between the prototype scale and the laboratory scale influence flow processes such as the 3D flow structures. However, conducting high quality field observations is challenging (Brown & Chanson, 2012, 2013), so such datasets remain very rare (Macchione et al., 2019). Rapidly evolving data mining techniques, based on crowdsourced data such as amateur videos (Kankanamge et al., 2020; Le Coz et al., 2016; Zhang et al., 2021), may unlock more widespread access to useable flow field observations at a prototype scale.

The current laboratory observations (flow depths, discharge partition, surface velocity) remain insufficient to comprehensively assess the reliability of the 3D flow structures predicted by 3D computations. Therefore, additional detailed laboratory measurements of 3D flow velocity are needed to advance the validation of 3D computational models.

Further research is needed to investigate additional processes which are not covered by the set of configurations tested here. This includes the influence of topographic effects, such as street width, steeper terrain slopes possibly leading to supercritical flow, and other geometric features typical of urbanized floodplains such as sidewalks (e.g., Bazin et al., 2017) and uneven bottom elevation in open spaces. Additional topics of interest include unsteady flooding scenarios (El Kadi Abderrezzak et al., 2009), flow exchanges between the streets and the urban drainage system (Chang et al., 2018; Hossain Anni et al., 2020; Martins et al., 2018; Rubinato et al., 2018) or flows entering the buildings (Mignot et al., 2020).

4. Conclusion

In this study, we compared flow depths, discharge partition and velocity fields computed with a 2D and a 3D model against laboratory experimental data obtained in a reduced-scale model of an urban district. Four distinct urban layouts were considered. The experimentally measured surface velocity fields were obtained with a large-scale particle image velocimetry technique.

Both the 2D and the 3D models compute flow depths in the inlet branches with an accuracy comparable to the experimental uncertainties, irrespective of the urban configuration. No significant difference was found between the flow depths predicted by the two models at the inlets, nor between the computed depth-averaged velocities in the inlet branches. Though, in all configurations, the 3D model underestimates the surface velocities by about 10% compared to the experiments.

The discharge partition between the outlets is predicted similarly by the two models, with differences between them comparable to the experimental uncertainties. The deviations between computed and observed outflow discharge fractions reach maximum four percent-points. This slightly exceeds the experimental uncertainty, which is estimated at maximum 2.5 percent-points. In configurations involving well-defined streets (CO, Px5), the 2D predictions agree slightly better with the observations, while in configurations with large open areas (CE and BD), the 3D model performs slightly better than the 2D model.

The 3D model overestimates surface velocity downstream of the *vena contracta* in branches located downstream of street intersections (Configurations CO and Px5), while the depth-averaged velocities computed by the 2D and the 3D models are remarkably consistent, apart from the close vicinity of the sidewalls. This suggests that the 2D model is generally reliable for predicting flow depths and discharge partition in urban districts, as well as depth-averaged flow velocities in street networks, that is, in the region where the flow is mostly channelized by the arrangement of obstacles such as rows of buildings. This finding appears to hold true despite the presence of helicoidal flow revealed by the 3D simulations.

In relatively large open areas (Configurations CE, Px5, and BD), the 3D model captures accurately the trajectory and velocity distribution of the main surface flow jet, except in a few localized areas (e.g., downstream end of the jet in Configuration CE), as well as the shape of experimentally observed surface flow recirculations. Discrepancies between computed and observed recirculation sizes exist but they remain limited. In contrast, the 2D model does not perform as well as it does in relatively channelized flow regions. The velocity magnitude in the recirculations is generally smaller in the 2D computations than it is in the laboratory observations and in the 3D results. In one case (middle part of Configuration Px5), even the side of jet reattachment is wrongly predicted by the 2D model, and this considerably alters the pattern of flow recirculations.

The difference between surface and depth-averaged velocities computed by the 3D model was examined as a potential indicator for pointing where a 3D model is necessary instead of a 2D one. While the magnitude of the differences between computed surface and depth-averaged velocities remains generally below 10% of the reference velocity, this magnitude reaches about 30% in regions located immediately downstream of street intersections as well as in some large open areas prone to flow velocity stratification (e.g., middle part of Configuration Px5). In the former case, the 2D model still performs accurately for predicting depth-averaged velocity, whereas it is not the case in the latter case. This hints at the fact that inspecting the deviations between surface and depth-average velocity is not a sufficient indicator for assessing the suitability of a 2D model.

Besides the hydrodynamic features analyzed in this study, the added value of 3D modeling should also be contemplated from the perspective of the multiple possible uses of the computed flow fields, such as modeling transport and mixing of contaminants or floating debris, assessing the stability of pedestrians, vehicles, or urban furniture, or modeling flood damage and monetary losses (Dottori et al., 2016; Molinari et al., 2020).

Finally, 3D modeling certainly offers new opportunities for taking full benefit of recent extremely high-resolution altimetry data (e.g., de Almeida et al. (2018)) and novel building information models (Rong et al., 2020), as well as for providing inputs for visualization of flooding scenarios in 3D-virtual environments for the sake of effective risk communication (Zhi et al., 2020).

Data Availability Statement

The datasets for this research are available in Li et al. (2022a). Supporting Information related to this article is available, including figures and tables.

Acknowledgments
This work was funded by the National Natural Science Foundation of China (No. 52309015) and Guangxi Science and Technology Major Project (No. AA23023009). This is also funded by the Guangxi Specific Research Project for Research Bases and Talents (No. AD23026176). The support from the French National Research Agency (ANR) for the project DEUFI (ANR-18-CE01-0020) is also acknowledged.

References

Arrault, A., Finaud-Guyot, P., Archambeau, P., Bruwier, M., Erpicum, S., Pirotton, M., & Dewals, B. (2016). Hydrodynamics of long-duration urban floods: Experiments and numerical modelling. *Natural Hazards and Earth System Sciences*, *16*(6), 1413–1429. 1413–1429-1413–1429. https://doi.org/10.5194/nhess-16-1413-2016

Bazin, P. H., Mignot, E., & Paquier, A. (2017). Computing flooding of crossroads with obstacles using a 2D numerical model. *Journal of Hydraulic Research*, *55*(1), 72–84. https://doi.org/10.1080/00221686.2016.1217947

Bosseler, B., Salomon, M., Schluter, M., & Rubinato, M. (2021). Living with urban flooding: A continuous learning process for local municipalities and lessons learnt from the 2021 events in Germany. *Water*, *13*(19), 2769. https://doi.org/10.3390/w13192769

Brown, R., & Chanson, H. (2012). Suspended sediment properties and suspended sediment flux estimates in an inundated urban environment during a major flood event. *Water Resources Research*, *48*(11). W11523-W11523. https://doi.org/10.1029/2012wr012381

Brown, R., & Chanson, H. (2013). Turbulence and suspended sediment measurements in an urban environment during the Brisbane River flood of January 2011. *Journal of Hydraulic Engineering*, *139*(2), 244–253. https://doi.org/10.1061/(asce)hy.1943-7900.0000666

Bruwier, M., Archambeau, P., Erpicum, S., Pirotton, M., & Dewals, B. (2017). Shallow-water models with anisotropic porosity and merging for flood modelling on Cartesian grids. *Journal of Hydrology*, *554*, 693–709. https://doi.org/10.1016/j.jhydrol.2017.09.051

Camnasio, E., Erpicum, S., Archambeau, P., Pirotton, M., & Dewals, B. (2014). Prediction of mean and turbulent kinetic energy in rectangular shallow reservoirs. *Engineering Applications of Computational Fluid Mechanics*, *8*(4), 586–597. https://doi.org/10.1080/19942060.2014.11083309

Chang, T.-J., Wang, C.-H., Chen, A. S., & Djordjević, S. (2018). The effect of inclusion of inlets in dual drainage modelling. *Journal of Hydrology*, *559*, 541–555. https://doi.org/10.1016/j.jhydrol.2018.01.066

Chen, X., Zhu, D. Z., & Steffler, P. M. (2017). Secondary currents induced mixing at channel confluences. *Canadian Journal of Civil Engineering*, *44*(12), 1071–1083. https://doi.org/10.1139/cjce-2016-0228

Chen, Y., Zhou, H., Zhang, H., Du, G., & Zhou, J. (2015). Urban flood risk warning under rapid urbanization. *Environmental Research*, *139*, 3–10. https://doi.org/10.1016/j.envres.2015.02.028

de Almeida, G. A. M., Bates, P., & Ozdemir, H. (2018). Modelling urban floods at submetre resolution: Challenges or opportunities for flood risk management? *Journal of Flood Risk Management*, *11*(S2), S855–S865. https://doi.org/10.1111/jfr3.12276

Dewals, B., Kitsikoudis, V., Angel Mejía-Morales, M., Archambeau, P., Mignot, E., Proust, S., et al. (2023). Can the 2D shallow water equations model flow intrusion into buildings during urban floods? *Journal of Hydrology*, *619*, 129231. https://doi.org/10.1016/j.jhydrol.2023.129231

Dottori, F., Di Baldassarre, G., & Todini, E. (2013). Detailed data is welcome, but with a pinch of salt: Accuracy, precision, and uncertainty in flood inundation modeling. *Water Resources Research*, *49*(9), 6079–6085. 6079–6085-6079–6085. https://doi.org/10.1002/wrcr.20406

Dottori, F., Figueiredo, R., Martina, M. L. V., Molinari, D., & Scorzini, A. R. (2016). INSYDE: A synthetic, probabilistic flood damage model based on explicit cost analysis. *Natural Hazards and Earth System Sciences*, *16*(12), 2577–2591. https://doi.org/10.5194/nhess-16-2577-2016

El Kadi Abderrezzak, K., Paquier, A., & Mignot, E. (2009). Modelling flash flood propagation in urban areas using a two-dimensional numerical model. *Natural Hazards*, *50*(3), 433–460. 433–460-433–460. https://doi.org/10.1007/s11069-008-9300-0

Erpicum, S., Meile, T., Dewals, B. J., Pirotton, M., & Schleiss, A. J. (2009). 2D numerical flow modeling in a macro-rough channel. *International Journal for Numerical Methods in Fluids*, *61*(11), 1227–1246. https://doi.org/10.1002/fld.2002

Fang, Q. (2016). Adapting Chinese cities to climate change. *Science*, *354*(6311), 425–426. 425–426-425–426. https://doi.org/10.1126/science.aak9826

Fekete, A., & Sandholz, S. (2021). Here comes the flood, but not failure? Lessons to learn after the heavy rain and pluvial floods in Germany 2021. *Water*, *13*(21), 3016. https://doi.org/10.3390/w13213016

Finaud-Guyot, P., Garambois, P. A., Araud, Q., Lawniczak, F., François, P., Vazquez, J., & Mosé, R. (2018). Experimental insight for flood flow repartition in urban areas. *Urban Water Journal*, *15*(3), 242–250. https://doi.org/10.1080/1573062x.2018.1433861

Finaud-Guyot, P., Garambois, P. A., Dellinger, G., Lawniczak, F., & François, P. (2019). Experimental characterization of various scale hydraulic signatures in a flooded branched street network. *Urban Water Journal*, *16*(9), 609–624. https://doi.org/10.1080/1573062x.2020.1713173

Güney, M. S., Tayfur, G., Bombar, G., & Elci, S. (2014). Distorted physical model to study sudden partial dam break flows in an urban area. *Journal of Hydraulic Engineering*, *140*(11). 05014006-05014006. https://doi.org/10.1061/(asce)hy.1943-7900.0000926

Guo, K. H., Guan, M. F., & Yu, D. P. (2021). Urban surface water flood modelling - A comprehensive review of current models and future challenges. *Hydrology and Earth System Sciences*, *25*(5), 2843–2860. https://doi.org/10.5194/hess-25-2843-2021

Guo, X., Cheng, J., Yin, C., Li, Q., Chen, R., & Fang, J. (2023). The extraordinary Zhengzhou flood of 7/20, 2021: How extreme weather and human response compounding to the disaster. *Cities*, *134*, 104168. https://doi.org/10.1016/j.cities.2022.104168

Hettiarachchi, S., Wasko, C., & Sharma, A. (2018). Increase in flood risk resulting from climate change in a developed urban watershed – The role of storm temporal patterns. *Hydrology and Earth System Sciences*, *22*(3), 2041–2056. https://doi.org/10.5194/hess-22-2041-2018

Hirt, C. W., & Nichols, B. D. (1981). Volume of fluid (VOF) method for the dynamics of free boundaries. *Journal of Computational Physics*, *39*(1), 201–225. https://doi.org/10.1016/0021-9991(81)90145-5

Hossain Anni, A., Cohen, S., & Praskievicz, S. (2020). Sensitivity of urban flood simulations to stormwater infrastructure and soil infiltration. *Journal of Hydrology*, *588*, 125028. https://doi.org/10.1016/j.jhydrol.2020.125028

Kankanamge, N., Yigitcanlar, T., Goonetilleke, A., & Kamruzzaman, M. (2020). Determining disaster severity through social media analysis: Testing the methodology with South East Queensland Flood tweets. *International Journal of Disaster Risk Reduction*, *42*, 101360. https://doi.org/10.1016/j.ijdrr.2019.101360

Kreibich, H., Thaler, T., Glade, T., & Molinari, D. (2019). Preface: Damage of natural hazards: Assessment and mitigation. *Natural Hazards and Earth System Sciences*, *19*(3), 551–554. 551–554-551–554. https://doi.org/10.5194/nhess-19-551-2019

Leandro, J., Schumann, A., & Pfister, A. (2016). A step towards considering the spatial heterogeneity of urban key features in urban hydrology flood modelling. *Journal of Hydrology*, *535*, 356–365. https://doi.org/10.1016/j.jhydrol.2016.01.060

Le Coz, J., Jodeau, M., Hauet, A., Marchand, B., & Le Boursicaud, R. (2014). Image-based velocity and discharge measurements in field and laboratory river engineering studies using the free FUDAA-LSPIV software. In *Proceedings of the International Conference on Fluvial Hydraulics (River Flow)*.

Le Coz, J., Patalano, A., Collins, D., Guillén, N. F., García, C. M., Smart, G. M., et al. (2016). Crowdsourced data for flood hydrology: Feedback from recent citizen science projects in Argentina, France and New Zealand. *Journal of Hydrology*, *541*, 766–777. https://doi.org/10.1016/j.jhydrol.2016.07.036

Li, X., Erpicum, S., Mignot, E., Archambeau, P., Pirotton, M., & Dewals, B. (2021). Influence of urban forms on long-duration urban flooding: Laboratory experiments and computation analysis. *Journal of Hydrology*, *603*, 127034. https://doi.org/10.1016/j.jhydrol.2021.127034

Li, X., Erpicum, S., Mignot, E., Archambeau, P., Pirotton, M., & Dewals, B. (2022a). Laboratory modelling of urban flooding. [Datasets]. *Zenodo*, *9*(1), 159. https://doi.org/10.5281/zenodo.5254164

Li, X., Erpicum, S., Mignot, E., Archambeau, P., Pirotton, M., & Dewals, B. (2022b). Laboratory modelling of urban flooding. *Scientific Data*, *9*(1), 159. https://doi.org/10.1038/s41597-022-01282-w

Li, X., Erpicum, S., Mignot, E., Archambeau, P., Rivière, N., Pirotton, M., & Dewals, B. (2020). Numerical insights into the effects of model geometric distortion in laboratory experiments of urban flooding. *Water Resources Research*, *56*(7), e2019WR026774–e022019WR026774. https://doi.org/10.1029/2019wr026774

Li, X., Kitsikoudis, V., Mignot, E., Archambeau, P., Pirotton, M., Dewals, B., & Erpicum, S. (2021). Experimental and numerical study of the effect of model geometric distortion on laboratory modeling of urban flooding. *Water Resources Research*, *57*(10), e2021WR029666. https://doi.org/10.1029/2021wr029666

Luo, H., Fytanidis, D. K., Schmidt, A. R., & Garcia, M. H. (2018). Comparative 1D and 3D numerical investigation of open-channel junction flows and energy losses. *Advances in Water Resources*, *117*, 120–139. https://doi.org/10.1016/j.advwatres.2018.05.012

Luo, P., Luo, M., Li, F., Qi, X., Huo, A., Wang, Z., et al. (2022). Urban flood numerical simulation: Research, methods and future perspectives. *Environmental Modelling and Software*, *156*, 105478. https://doi.org/10.1016/j.envsoft.2022.105478

Lv, H., Wu, Z., Meng, Y., Guan, X., Wang, H., Zhang, X., & Ma, B. (2022). Optimal domain scale for stochastic urban flood damage assessment considering triple spatial uncertainties. *Water Resources Research*, *58*(7), e2021WR031552. https://doi.org/10.1029/2021WR031552

Macchione, F., Costabile, P., Costanzo, C., & Lorenzo, G. D. (2019). Extracting quantitative data from non-conventional information for the hydraulic reconstruction of past urban flood events. A case study. *Journal of Hydrology*, *576*, 443–465. https://doi.org/10.1016/j.jhydrol.2019.06.031

Martins, R., Rubinato, M., Kesserwani, G., Leandro, J., Djordjevic, S., & Shucksmith, J. D. (2018). On the characteristics of velocities fields in the vicinity of manhole inlet grates during flood events. *Water Resources Research*, *54*(9), 6408–6422. https://doi.org/10.1029/2018wr022782

Mejía-Morales, M. A., Mignot, E., Paquier, A., & Proust, S. (2023). Laboratory investigation into the effect of the storage capacity of a city block on unsteady urban flood flows. *Water Resources Research*, *59*(4), e2022WR032984. https://doi.org/10.1029/2022WR032984

Mejia-Morales, M. A., Mignot, E., Paquier, A., Sigaud, D., & Proust, S. (2021). Impact of the porosity of an urban block on the flood risk assessment: A laboratory experiment. *Journal of Hydrology*, *602*, 126715–126715. https://doi.org/10.1016/j.jhydrol.2021.126715

Mignot, E., Bonakdari, H., Knothe, P., Kouyi, G. L., Bessette, A., Riviere, N., & Bertrand-Krajewski, J. L. (2012). Experiments and 3D simulations of flow structures in junctions and their influence on location of flowmeters. *Water Science and Technology*, *66*(6), 1325–1332. https://doi.org/10.2166/wst.2012.319

Mignot, E., Camusson, L., & Riviere, N. (2020). Measuring the flow intrusion towards building areas during urban floods: Impact of the obstacles located in the streets and on the facade. *Journal of Hydrology*, *583*, 124607–124607. https://doi.org/10.1016/j.jhydrol.2020.124607

Mignot, E., & Dewals, B. (2022). Hydraulic modelling of inland urban flooding: Recent advances. *Journal of Hydrology*, *609*, 127763. https://doi.org/10.1016/j.jhydrol.2022.127763

Mignot, E., Paquier, A., & Haider, S. (2006). Modeling floods in a dense urban area using 2D shallow water equations. *Journal of Hydrology*, *327*(1), 186–199. https://doi.org/10.1016/j.jhydrol.2005.11.026

Mignot, E., Zeng, C., Dominguez, G., Li, C. W., Rivière, N., & Bazin, P. H. (2013). Impact of topographic obstacles on the discharge distribution in open-channel bifurcations. *Journal of Hydrology*, *494*, 10–19. https://doi.org/10.1016/j.jhydrol.2013.04.023

Molinari, D., Scorzini, A. R., Arrighi, C., Carisi, F., Castelli, F., Domeneghetti, A., et al. (2020). Are flood damage models converging to "reality"? Lessons learnt from a blind test. *Natural Hazards and Earth System Sciences*, *20*(11), 2997–3017. 2997–3017-2997–3017. https://doi.org/10.5194/nhess-20-2997-2020

Momplot, A., Kouyi, G. L., Mignot, E., Rivière, N., & Bertrand-Krajewski, J.-L. (2017). Typology of the flow structures in dividing open channel flows. *Journal of Hydraulic Research*, *55*(1), 63–71. https://doi.org/10.1080/00221686.2016.1212409

Paquier, A., Bazin, P.-H., & El Kadi Abderrezzak, K. (2020). Sensitivity of 2D hydrodynamic modelling of urban floods to the forcing inputs: Lessons from two field cases. *Urban Water Journal*, *17*(5), 457–466. https://doi.org/10.1080/1573062x.2019.1669200

Rong, Y., Zhang, T., Zheng, Y., Hu, C., Peng, L., & Feng, P. (2020). Three-dimensional urban flood inundation simulation based on digital aerial photogrammetry. *Journal of Hydrology*, *584*, 124308–124308. https://doi.org/10.1016/j.jhydrol.2019.124308

Rosenzweig, B. R., Herreros Cantis, P., Kim, Y., Cohn, A., Grove, K., Brock, J., et al. (2021). The value of urban flood modeling. *Earth's Future*, *9*(1), e2020EF001739. https://doi.org/10.1029/2020EF001739

Rubinato, M., Lee, S., Martins, R., & Shucksmith, J. D. (2018). Surface to sewer flow exchange through circular inlets during urban flood conditions. *Journal of Hydroinformatics*, *20*(3), 564–576. https://doi.org/10.2166/hydro.2018.127

Schindfessel, L., Creëlle, S., & De Mulder, T. (2015). Flow patterns in an open channel confluence with increasingly dominant tributary inflow. *Water*, *7*(9), 4724–4751. 4724–4751-4724–4751. https://doi.org/10.3390/w7094724

Smith, G. P., Rahman, P. F., & Wasko, C. (2016). A comprehensive urban floodplain dataset for model benchmarking. *International Journal of River Basin Management*, *14*(3), 345–356. https://doi.org/10.1080/15715124.2016.1193510

Testa, G., Zuccala, D., Alcrudo, F., Mulet, J., & Soares-Frazão, S. (2007). Flash flood flow experiment in a simplified urban district. *Journal of Hydraulic Research*, *45*(SPEC. ISS.), 37–44. https://doi.org/10.1080/00221686.2007.9521831

Torres, C., Borman, D., Matos, J., & Neeve, D. (2022). CFD modeling of scale effects on free-surface flow over a labyrinth weir and spillway. *Journal of Hydraulic Engineering*, *148*(7), 04022011. https://doi.org/10.1061/(ASCE)HY.1943-7900.0001989

Velickovic, M., Zech, Y., & Soares-Frazão, S. (2017). Steady-flow experiments in urban areas and anisotropic porosity model. *Journal of Hydraulic Research*, *55*(1), 85–100. https://doi.org/10.1080/00221686.2016.1238013

Versteeg, H., & Malalasekera, W. (2007). An introduction to computational fluid dynamics: The finite volume method/H. K. Versteeg and W. Malalasekera. *SERBIU*LA (sistema Librum 2.0).

Weber, L. J., Schumate, E. D., & Mawer, N. (2001). Experiments on flow at a 90° open-channel junction. *Journal of Hydraulic Engineering*, *127*(5), 340–350. https://doi.org/10.1061/(asce)0733-9429(2001)127:5(340)

Yuan, S., Tang, H., Xiao, Y., Qiu, X., & Xia, Y. (2018). Water flow and sediment transport at open-channel confluences: An experimental study. *Journal of Hydraulic Research*, *56*(3), 333–350. https://doi.org/10.1080/00221686.2017.1354932

Zhang, Y., Chen, Z., Zheng, X., Chen, N., & Wang, Y. (2021). Extracting the location of flooding events in urban systems and analyzing the semantic risk using social sensing data. *Journal of Hydrology*, *603*, 127053. https://doi.org/10.1016/j.jhydrol.2021.127053

Zhi, G., Liao, Z., Tian, W., & Wu, J. (2020). Urban flood risk assessment and analysis with a 3D visualization method coupling the PP-PSO algorithm and building data. *Journal of Environmental Management*, *268*, 110521–110521. https://doi.org/10.1016/j.jenvman.2020.110521

Zhu, X., & Lipeme Kouyi, G. (2019). An analysis of LSPIV-based surface velocity measurement techniques for stormwater detention basin management. *Water Resources Research*, *55*(2), 888–903. https://doi.org/10.1029/2018wr023813

Zhu, Z., Gou, L., Liu, S., & Peng, D. (2023). Effect of urban neighbourhood layout on the flood intrusion rate of residential buildings and associated risk for pedestrians. *Sustainable Cities and Society*, *92*, 104485. https://doi.org/10.1016/j.scs.2023.104485